# WASp activity in macrophages prevents mechano-induced inflammation by protecting the nuclear envelope

Roberto Amadio[1,2], Giulia Bracchetti[1], Zahraa Alraies[3,#], Giulia Maria Piperno[1], Lucia Lopez Rodriguez[1], Mathieu Maurin[3], Martina Conti[4], Laura Andolfi[4], Maria Carmina Castiello[5,6], Francesca Ferrua[5], Anna Villa[5,6], Alessandro Aiuti[5], Ana-Maria Lennon-Dumenil[3] and Federica Benvenuti[1,*]

[1]Cellular Immunology, International Centre for Genetic Engineering and Biotechnology (ICGEB), Trieste, Italy

[2]University of Trieste, Department of Life Sciences (DSV), 34127 Trieste, Italy

[3]INSERM-U932 Immunité et Cancer, Institut Curie, PLS Research University, 75005 Paris, France

[4]Istituto Officina dei Materiali - National Research Council (CNR-IOM) - Basovizza, Trieste, Italy

[5]San Raffaele Telethon Institute for Gene Therapy (SR-TIGET), IRCSS San Raffaele Scientific Institute, 20132 Milan, Italy

[6]Institute for Biomedical Technologies - National Research Council (CNR-ITB), 20054 Segrate, Milan, Italy

[#]Present address: Laboratory of Cell and Molecular Biology, Experimental Research (C1), 005E - NYU Abu Dhabi, Saadiyat Campus, Abu Dhabi, United Arab Emirates

*Corresponding author, Federica Benvenuti, benvenut@icgeb.org

## Abstract

Mutations in the immune-specific actin regulator WASp induce a proinflammatory state in myeloid cells, whose underlying causes remain poorly defined. Here, we applied microfabricated tools that mimic tissue mechanical forces to explore the role of WASp in connecting mechano-sensing to the activation of inflammatory responses in macrophages. We show that WASp-deficient macrophages carry alterations in nuclear structure and undergo increased blebbing and nuclear rupture when exposed to mechanical confinement. High-resolution imaging indicates that WASp drives the formation of protective perinuclear actin structures in response to confinement. Functionally, a proinflammatory gene signature linked to nuclear envelope rupture is preferentially active in confined WASp null macrophages, which partially depends on the cGAS-STING pathway of cytosolic DNA sensing. Analysis of transcriptional datasets of human and mouse tissue macrophages confirmed elevated inflammatory activation in WASp null cells. Together, these data uncover that WASp restricts pro-inflammatory activation of macrophages by preserving nuclear integrity in confined environments, providing novel clues to understand inflammatory activation in Wiskott-Aldrich Syndrome.

**Running title**: Branched actin polymerization in control of nuclear integrity and inflammation

**Keywords**: Wiskott-Aldrich Syndrome, actin, macrophages, nuclear rupture, inflammation

**ORCIDs and e-mails**:
R.A: 0000-0003-0861-0703, roberto.amadio@icgeb.org

## Introduction

Tissue mechanical forces are emerging as key orchestrators of inflammation and immune responses in homeostatic and pathological conditions. Depending on the context, tissue rigidity and compression are transduced by diverse mechanisms to enhance or dampen cytokine production (Jain and Vogel, 2018; Du et al., 2022). Mechanical inputs are received by the nucleus, the larger and more rigid cellular organelle, through a complex connection between the nuclear lamina and the cytoskeleton, inducing morphological changes that regulate chromatin organisation and gene transcription (Nader et al., 2021b). However, errors in transmission or reception of mechanical cues may cause loss of nuclear envelope integrity and unwanted extrusion of chromosomal DNA into the cytosol (Härtlova et al., 2015; Dou et al., 2017; Dunphy et al., 2018), which is detected by cytosolic sensors such as cGAS and STING. Engagement of such receptors, triggers activation of cytokine genes, senescence or cell death, depending on the severity of damage (Dou et al., 2017; Mu et al., 2020; Nader et al., 2021a; Sladitschek-Martens et al., 2022), which may promote development of autoimmunity (Decout et al., 2021). Hence, maintaining nuclear envelope integrity is critical to restrict unwanted activation, particularly in immune cells that navigate complex environments, and are continuously exposed to mechanical compression (Denais et al., 2016; Raab et al., 2016; De Silva et al., 2023). Nuclear stability relies on a finely regulated balance between chromatin mechanics and cytoskeletal forces (Nava et al., 2020). Within cytoskeletal components, microtubules were shown to limit nuclear deformations in dendritic cells (Thiam et al., 2016), while intermediate filaments protect nuclei of murine embryonic fibroblast during constricted migration (Patteson et al., 2019). Arp2/3-dependent branched actin polymerization is critical to support nuclear deformation in migrating dendritic cells (Thiam et al., 2016) , and it acts as a barrier to maintain nuclear integrity and limit DNA damage (Sladitschek-Martens et al., 2022; Delgado et al., 2024). Consistently, genetic ablation of the Cdc42 GTPase DOCK8 impairs nuclear integrity in T and dendritic cells during confined migration (Reis-rodrigues et al., 2024; Shen et al., 2024), suggesting that a broad range of diseases caused by mutations in regulators of actin branching may suffer from nuclear derangement.

The Wiskott-Aldrich Syndrome (WAS) is a primary immunodeficiency characterized by frequent autoimmune and autoinflammatory manifestations. WAS is caused by mutations in Wiskott-Aldrich Syndrome protein (WASp), a critical activator of the Arp2/3 complex which controls branched actin polymerization specifically in non-erythroid immune cells (Blundell et al., 2010; Naseem et al., 2022). WASp expression in immune cells regulates actin-driven processes such as cell migration (Gaertner et al., 2022; Oliveira et al., 2022), bacterial clearance (Lee et al., 2017), cytokine production (Prete

et al., 2013; Cervantes-Luevano et al., 2018; Piperno et al., 2020; Amadio et al., 2021) and homeostasis of autoreactive B cells and Tregs (Sereni et al., 2018; Calixto Vieira et al., 2023). However, whether WASp plays a role in nuclear integrity is unknown. This may be particularly relevant in myeloid cells that experience continuous mechanical challenges in tissues and were shown to display and increased inflammatory phenotype in WAS.

In this work, we applied microfabricated tools that mimic tissues' mechanical forces to address the role of WASp in preserving nuclear stability and inflammatory responses under mechanical pressure. By combining imaging and transcriptional profiling, we found that WASp-driven actin polymerization is necessary to counteract mechanical challenges and preserve nuclear envelope integrity in macrophages, restricting inflammatory activation.

## Results

### Nuclear defects in WKO macrophages

To explore the hypothesis of an altered nuclear phenotype in WAS, we started by analysing simple nuclear parameters in bone marrow derived macrophages derived from wild type or WASp null mice (WT and WKO hereafter) (Snapper et al., 1998; Prete et al., 2013). We assessed the area, roundness and presence of micronuclei in cells plated in 2D (Fig.1A). We found that the nuclei of WKO macrophages had an increased mean projected area, were more irregular and showed a higher incidence of micronuclei (Fig.1B), indicating general alterations in nuclear homeostasis. Previous findings in other systems linked defects in Lmna (encoding for Lamin A/C) and nuclear envelope folding to impaired mechanical tension and reduced protection from deformations (Kim et al., 2017; Tang et al., 2023). We thus focused on Lamin A/C and the nuclear envelope protein Emerin in our model. Total Lamin A/C levels were reduced in WKO, both at the protein and mRNA level, whereas mRNA expression of type B lamins and Emerin was not different (Fig.1C and 1D). Importantly, we noticed higher degree of Lamin A/C wrinkles and irregularities in nuclei of WASp null macrophages (Fig.1E), which coincided with Emerin accumulation (Fig.1F). Altogether these data suggest defective nuclear envelope homeostasis and increased folding of the nuclear envelope in the absence of WASp.

Next, as the nucleus is highly connected to chromatin and cellular mechanics, we explored chromatin parameters and global cellular stiffness. We did not observe substantial differences in global heterochromatin content and peripheral heterochromatin between the two genotypes by chromocenters analysis (Supplemental Fig.1A). Similarly, no changes in heterochromatin distribution were detected by H3K9me2 staining, but we observed an increase in the total intensity of this marker (Supplemental Fig.1B). Cellular mechanics, as measured by Atomic Force Microscopy (AFM) indentation (Supplementary Fig.1C) showed that WKO cells were stiffer than WT ones (Supplementary Fig.1D). Of note, a stiffer cytoplasm has been linked to reduced nuclear stability under 3D physical constrains (Bastianello et al., 2023).

### Increased constricted migration and nuclear deformation in WKO macrophages

Next, we addressed the role of WASp in controlling the mechanical properties of the nucleus. First, we performed an assay to force nuclear deformations inside narrow constrictions using microchannels (Vargas et al., 2016). We adopted different channel dimensions, ranging from 2 µm

159 to 8 µm in width and having a constant height of 5 µm. Macrophages were seeded in the pre-channel
160 chamber and recorded overnight. The number of cells that entered the channel was calculated at
161 the end of the recording period by counting the number of cells inside channels and normalizing by
162 the number of approaching cells (Supplementary Fig.2A; materials and methods). As expected,
163 reducing the size of the channels inhibited the entrance of cells inside constrictions (Fig.2A).
164 Interestingly, the entrance rate of WKO macrophages was consistently higher, especially at smaller
165 constrictions (Fig.2B). By carefully inspecting nuclear shape in cells inside channels we observed
166 enhanced frequencies of nuclear herniations in WKO (Fig.2C). Herniations were preferentially
167 observed at the front of the cell in the direction of migration (Fig.2D), in line with previous
168 observations in other cell types (Denais et al., 2016). Since herniations predispose to nuclear
169 rupture, we next transduced macrophages with a lentiviral construct expressing a nuclear
170 localization signal (NLS)-tagged GFP (NLS–GFP), which is retained inside the nucleus and it is released
171 upon nuclear envelope (NE) rupture (Fig.2E). Interestingly, we observed a larger fraction of NE
172 rupture and cytosolic release of fluorescent signal in WKO macrophages than in WT (Fig.2F and 2G).
173 Moreover, and consistently with increased nuclear fragility, we detected multiple rupture events on
174 the same cell exclusively in WKO (Fig.2H). A parallel set of transwell migration experiments
175 confirmed the superior ability of WASp null cells to translocate through small pores (Supplementary
176 Fig.2B). We ruled out that enhanced transwell migration in WKO may depend on changes in
177 chemokine receptors expression (Supplementary Fig.2C). Notably, migration induced an increase in
178 nuclear deformation and enhanced γH2AX staining, particularly in WKO cells (Supplementary
179 Fig.2D). Overall, these data indicate that WASp-deficient macrophages are facilitated in entering
180 small constriction, in line with a previous report on dendritic cells (Gaertner et al., 2022), suggesting
181 reduced resistance to nuclear deformation. Importantly, the nuclear envelope of WKO cells ruptures
182 during constricted migration, releasing nuclear material into the cytosol.
183
184 **WASp limits nuclear ruptures under mechanical confinement**
185 To more faithfully recapitulate deformation events experienced by macrophages in tissues, we next
186 applied a vertical confiner device (Alraies et al., 2024) based on PDMS micropillars (Supplementary
187 Fig.3A). The heights of BMDM nuclei plated on fibronectin-coated glass slides without confinement
188 range between 5 and 6 µm (Supplementary Fig.3B), therefore we selected 6 and 3 µm height as mild
189 and strong confinement, respectively (Supplementary Fig.3C). Confocal images were acquired after
190 one hour of confinement to examine nuclear parameters. We classified nuclei into two categories:

191 1) intact, when the nuclear boundaries were regular and continuous; 2) damaged, when blebs or
192 herniations were found to interrupt the nuclear perimeter (Fig.3A). The fraction of damaged nuclei
193 in WASp null cells was slightly higher under mild confinement and significantly higher under strong
194 confinement (Fig.3B), suggesting loss of nuclear integrity. Indeed, measuring NLS-GFP localization
195 after confinement at 3 µm, we observed an increased frequency of NE rupture and NLS-GFP cytosolic
196 release in WKO cells (Fig.3C and 3D). Live tracking of NLS-GFP leakage revealed that rupture
197 correlates to blebbing/herniation of the nuclear surface (Fig.3E). To causally link WASp to nuclear
198 deformation and loss of NE integrity, we next transduced WASp null macrophages with a lentiviral
199 construct expressing WASp-GFP (Supplementary Fig.3D) (Blundell et al., 2008). This resulted in
200 around 50% of cells expressing a clear GFP signal and WASp-GFP fusion protein of the expected size
201 (Supplementary Fig. 3E and 3F). The resulting mixed population of GFP-positive (rescued) and
202 negative (control) cells were subjected to confinement at 3 µm. In this highly controlled setting, we
203 found that GFP-positive cells showed significantly fewer nuclear blebs than GFP-negative ones (Fig.
204 3F and 3G). Moreover, the fraction of cells showing Lamin A/C rupture was reduced in WASp-GFP
205 positive cells (Fig.3H and 3I), confirming a direct impact of WASp in preserving nuclear stability under
206 confinement.
207
208 **WASp directs perinuclear actin polymerization in confined macrophages**
209 We then aimed to investigate a potential mechanism by which WASp and actin polymerization
210 support nuclear stability during mechanical challenges. We took advantage of a fixation-under-
211 confinement protocol, which preserves cytoskeletal structures once confinement is released (Alraies
212 et al., 2024). We found that confinement triggered the accumulation of dense actin structures in the
213 central body of the cell in WT, but not in WKO macrophages (Fig.4A). These actin patches closely
214 resemble the Arp2/3-dependent structures described in mechanically confined dendritic cells with
215 a role in nuclear envelope unfolding (Alraies et al., 2024). By high-resolution imaging, we further
216 classified confined cells into four categories according to actin distribution: 1) perinuclear actin
217 patches; 2) intranuclear actin accumulation; 3) filamentous perinuclear actin ring and 4) diffuse
218 cytosolic actin (Fig.4B). Of note, perinuclear actin patches were observed in a substantial proportion
219 of WT cells but were virtually absent in WKO (Fig.4C and 4D). Intranuclear actin accumulation was
220 present in a small fraction of cells, in similar frequencies between the two genotypes. Additionally,
221 a small fraction of WKO cells showed thin filamentous actin surrounding the nucleus (Fig.4C and 4D),
222 a phenomenon not detected in WT macrophages. To explore the role of WASp in driving the

223 polymerization of perinuclear actin structures, we leveraged WKO macrophages transduced with
224 WASp-GFP for colocalization analysis (Fig.4E). Interestingly, the Mander's coefficient between
225 phalloidin and GFP was high in the perinuclear actin patches induced by confinement (Fig.4F),
226 strongly suggesting an active role of WASp in directing the formation of these structures.
227 Consistently, also the distribution of WASp-GFP in macrophages inside microchannels was enriched
228 in the central part of the cell body and around the nucleus (Supplementary Fig.4A and 4B). We
229 conclude that WASp drives the nucleation of perinuclear actin patches in macrophages exposed to
230 mechanical confinement. Together with the previous observations, this result suggests that a local
231 perinuclear actin response may help to preserve nuclear integrity.
232
233 **Confinement-induced nuclear ruptures exacerbate inflammation in WKO macrophages**
234 To investigate the functional consequences of increased nuclear fragility in WASp null macrophages,
235 we then analysed transcriptional changes induced by confinement (Fig.5A). WT and WKO
236 macrophages at steady state (unconfined) express a common transcriptional program and some
237 genotype-specific genes (Supplementary Fig.5A). Remarkably, WKO cells were enriched in
238 immunoglobulin coding genes, an observation that deserves future investigations. Moreover,
239 transcripts related to extracellular matrix organization, vascular remodelling and cellular
240 activation/migration were higher in unconfined WKO macrophages than in WT. In contrast, genes
241 controlling cellular metabolism were less expressed in WKO (Supplementary Fig.5A and
242 Supplementary Table 1). Confinement induced profound transcriptional remodelling in both
243 genotypes (Supplementary Fig.5B). Analysis of differentially expressed genes (DEGs) between
244 unconfined and confined cells unveiled a core of 130 genes commonly upregulated by confinement
245 in WT and WKO (Fig.5B), including some inflammatory cytokines and chemokines (Fig.5C). In
246 addition, we observed 151 genes upregulated only in confined WKO cells and 36 in WT cells.
247 Interestingly, genes selectively upregulated in WKO were related to inflammatory activation and
248 tissue remodelling (Fig.5B), paralleled by reduced expression of metabolic pathways (Supplementary
249 Fig.5C).
250 To explore the molecular mechanisms underlying cellular responses to confinement, we evaluated
251 the expression of genes implicated in cytoskeletal dynamics and control of nuclear stability
252 (Supplementary Table 2), across all the conditions. A signature encompassing genes that control
253 actin branching (branched actin score) was significantly higher in WT than in WKO macrophages,
254 suggesting that WASp deficiency broadly impacts this process. Upon confinement, this gene set was

255 upregulated in both genotypes, indicating fast cellular adaptation to mechanical inputs (Fig.5D),
256 however it remained lower in WKO cells. This trend was even more prominent when selecting
257 specific WASp effectors that have been directly linked to NE integrity (*Actr2*, *Actr3*, *Arpc4*)
258 (Sladitschek-Martens et al., 2022; Delgado et al., 2024); showing a drastic reduction of expression in
259 both unconfined and confined WASp deficient cells. Of note, a second gene module linked to nuclear
260 mechanics including several genes previously implicated in NE stability, such as Lamin A/C, Emerin
261 and Lap2β (Tmpo) (Chen et al., 2021; Lavenus et al., 2022; De Silva et al., 2023) was significantly
262 upregulated in WT cells, but not in WKO, upon confinement (Fig.5E). Conversely, SUN2 and
263 RhoA/ROCK, whose overexpression has been linked to nuclear blebbing and innate activation (Mu
264 et al., 2020), were higher in WKO cells, together with RAC2-related genes (Supplementary Fig.5D).
265 All together, these data suggest a defective branched actin-based response to confinement in WKO
266 macrophages, concomitant to induction of a compensatory RhoA/RAC-mediated pathway, with a
267 potentially negative impact on nuclear stability.
268 Defective mechanotransduction and reduction in the expression of genes linked to actin-dependent
269 nuclear integrity were previously shown to induce activation of a proinflammatory cell state in
270 Arp2/3 deficient fibroblast (Sladitschek-Martens et al., 2022). Hence, we examined the expression
271 of this signature, defined as "nuclear envelope rupture (NER) inflammatory score" in our dataset.
272 Remarkably, the NER inflammatory score was selectively activated in confined WASp null
273 macrophages, causally connecting WASp to the control of proinflammatory activation in cells
274 exposed to mechanical inputs (Fig.5F). Among the genes included in NER inflammatory score, Il6 was
275 selected to perform further functional analyses. qPCR confirmed that Il6 transcripts were
276 preferentially induced by confinement in WKO (Fig.5G). To exclude any potential bias in macrophages
277 derived from constitutive WASp KO animals, we induced acute WASp deletion in WT BMDM by
278 CRISPR-Cas9 gene editing (Supplementary Fig.5E). Importantly, WASp-depleted macrophages
279 responded to confinement by augmented Il6 induction as compared to control cells (Fig.5H),
280 indicating that WASp directly restricts confinement-induced activation. Given the widespread
281 implications of the cGAS-STING pathway of cytosolic DNA sensing (Ablasser and Gulen, 2016) to
282 innate activation and specifically in driving the NER inflammatory score (Sladitschek-Martens et al.,
283 2022), we assessed its contribution to confinement-induced activation of WKO cells. STING ablation
284 in WKO macrophages (Supplementary Fig.5F) blunted Il6 production upon direct stimulation by
285 DMXAA, confirming the functional disruption of the pathway (Supplementary Fig.5G). We then
286 exposed WKO macrophages carrying or not STING depletion to confinement at 3 µm of height.

287 Induction of Il6 transcripts was significantly reduced in WKO STING KO macrophages as compared to
288 STING-proficient cells, causally connecting the pathway to the proinflammatory state of WKO
289 macrophages (Fig.5I). Nevertheless, the uncomplete inhibition of Il6 expression in STING-depleted
290 cells suggests that other sensors/mechanisms may contribute to the inflammatory activation
291 downstream of NE ruptures in WASp-deficient cells. We conclude that increased NE rupture in WASp
292 null macrophages triggers the expression of a specific proinflammatory signature (Fig.5J).
293
294 **Inflammatory phenotype in mouse and human WASp deficient macrophages**
295 To validate our findings *in-vivo* we next focused on lung alveolar macrophages (AMO), a
296 representative population of long-lasting resident macrophages constantly exposed to physical
297 constraints and subjected to almost 2D confinements (De Silva et al., 2023). Flow cytometry profiling
298 of AMO (Supplementary Fig.6A), showed higher levels of the activation marker CD86 in WKO mice
299 (10 weeks of age), as compared to WT (Fig.6A). We next isolated AMO from 10 weeks and 25 weeks
300 old mice. The absolute number of AMO was higher in WKO as compared to controls, especially at 25
301 weeks of age (Fig.6B). Notably, Il6 transcripts were slightly elevated in young animals and
302 significantly higher in AMO from 25 weeks old WKO mice (Fig.6C). Therefore, we conclude that WASp
303 is dispensable for differentiation or survival of lung tissue resident macrophages, however it controls
304 their homeostatic inflammatory state.
305 To translate the importance of macrophage activation to humans, we designed an inflammatory
306 signature (Inflammatory score, Supplementary Table 3) and used it to interrogate two different data
307 sets. First, we re-analysed a publicly available dataset of WAS iPSCs-derived macrophages
308 (GSE107963, TPM normalized reads), and their isogenic counterparts that have been corrected to
309 re-express WASp (Yuan et al., 2022). Despite high variations among samples, we found the
310 expression of the inflammatory score is inversely correlated to WASp expression (Fig.6D).
311 Remarkably, some genes within the NER signature (*Il6, Ccl8, Cxcl10 and Ctsb)* were consistently
312 reduced by reintroducing WASp. The same trend was observed for other genes in the signature,
313 albeit less consistently (Fig 6E). Moreover, those nuclear mechanics related genes controlled by
314 WASp in mouse macrophages, were consistently lower in WASp mutated human macrophages
315 (Fig.6F).
316 We also performed a bulk RNA-seq on PBMCs from a cohort of 6 WAS patients that were treated by
317 gene therapy at SR-TIGET. Major WAS defects (i.e. BCR signalling and genes related to platelets
318 function) were normalized post gene therapy (post-GT), without inducing alteration in other Arp2/3

319 activators (Supplementary Fig.6B and C). Interestingly, despite the complex composition of PBMCs
320 that comprises several subsets (mainly B, T, NK and monocytes) and patients' heterogeneity, we
321 observed a consistent decrease in the inflammatory score post-GT (Fig.6G). Selected inflammatory
322 genes emerging from RNA-seq, were validated by RT-qPCR, confirming that re-introducing WASp is
323 sufficient to normalize inflammatory gene expression to the level of healthy donors (Supplementary
324 Fig.6D). Intriguingly, the overall correction index was greater in samples showing a higher basal level
325 of inflammation (Supplementary Fig.6E). In line with previous results, the NER signature score was
326 elevated in five out of six patients, with some specific genes (Il6, *Ctsb, Ccl3, Cxcl10*) strongly
327 depending on WASp expression (Fig 6H). These results support a role for WASp in restraining the
328 inflammatory activation of human macrophages and, possibly, of other immune subsets.
329
330

331 **Discussion**

332 Biophysical cues expressed in tissues influence the inflammatory functions of macrophages by a
333 range of cellular mechanisms, including mechanotransduction at the nuclear envelope. In this study
334 we show that WASp acts as a barrier to avoid nuclear rupture in mechanically challenged
335 macrophages, restraining inflammatory responses. This direct connection between WASp-mediated
336 actin polymerization and nuclear integrity has emerged from an experimental setup that
337 recapitulates tissue forces experienced by cells *in-vivo.* Hence, this approach uncovered an essential
338 supplementary function for the hematopoietic-specific actin nucleation-promoting factors WASp,
339 beyond the well-established role at the cell cortex and in intracellular trafficking (Linder et al., 1999;
340 Piperno et al., 2020; Gaertner et al., 2022). These findings are particularly relevant given the
341 intrinsically migratory nature of immune cells and the nucleus as the main rate-limiting factor for
342 constricted migration.
343

344 Previous studies showed that WASp null dendritic cells migrate faster inside microchannels or
345 through non-deformable constrictions. However, the findings were not interpreted as dependent on
346 altered nuclear properties (Gaertner et al., 2022; Oliveira et al., 2022). Our analysis confirms that
347 WASp null macrophages, likewise dendritic cells, are facilitated in entering small constrictions.
348 Additionally, we demonstrate that this is linked to an enhanced ability of the nucleus to deform,
349 which correlates to a predisposition to undergo nuclear rupture. Cells harbouring defects in Lamin
350 A/C or a disrupted nuclear-cytoskeleton coupling show similar nuclear deformations, increased

351 migration and high rates of nuclear ruptures when exposed to mechanical confinement (Davidson
352 et al., 2014; Harada et al., 2014; Kim et al., 2017; Bell et al., 2022). In line with our findings, a parallel
353 study by our collaborators observed increased nuclear deformation and ruptures in confined
354 dendritic cells that lack the WASp effector Arp2/3 (Delgado et al., 2024). More than one mechanism,
355 not mutually exclusive, may explain reduced nuclear integrity in WASp null cells. The dense F-actin
356 patches formed upon confinement and the immediate transcriptional response to supply factors
357 controlling actin branching in WT, but not in WKO cells, suggest that WASp may induce cytoskeletal
358 remodelling downstream of mechanical stimuli, creating a protective perinuclear actin barrier.
359 Alternatively, as suggested by the presence of thin actin rings around the nucleus of a fraction of
360 WKO cells and by gene expression data, lack of WASp may drive compensatory actin polymerization
361 by different factors. As documented in a previous report, the resulting abnormal actin network may
362 cause rupture by exerting excessive pressure on the NE under confinement (Mu et al., 2020).
363 Interestingly, similar perinuclear actin rings were also observed in epithelial cells upon mechanical
364 stretching, which has a role in promoting chromatin compaction (Le et al., 2016). Moreover, we
365 cannot exclude that WASp limits nuclear rupture by acting inside the nucleus(Caridi et al., 2019),
366 protecting it from DNA damage (Kovacs et al., 2023) or by mediating DNA repair dynamics via Arp2/3
367 (Delgado et al., 2024).
368 Of note, despite mild Lamin A/C defects and slight accumulation of DNA damage in WASp null
369 macrophages, we found that the number of tissue-resident cells *in-vivo* was not affected, as opposed
370 to the phenotype in Arpc4 KO and Lamin A/C deficient animals where Langerhans cells and alveolar
371 macrophages, respectively, are depleted in tissues (De Silva et al., 2023; Delgado et al., 2024).
372 Therefore, WASp ablation induces a proinflammatory state that does not culminate in cell death,
373 suggesting a milder phenotype than complete blockade of Arp2/3 or Lamin A/C deletion. Whether
374 this results from compensation by other NPFs remains to be investigated.
375 The unscheduled release of genomic DNA into the cytosol has been documented consequently to
376 DNA damage (Dunphy et al., 2018; Mukherjee et al., 2019; Song et al., 2021), defective Lamin A/C
377 (De Silva et al., 2023; En et al., 2024) and disrupted mechano-signalling due to reduced expression
378 of Arp2/3, a direct WASp effector (Sladitschek-Martens et al., 2022). The latter study associated
379 nuclear instability and nuclear envelope rupture to cGAS-STING activation and senescence in
380 fibroblast. We observed a similar inflammatory activation downstream of NE rupture in WKO, raising
381 many interesting points. While STING predominantly activates IRF3 upon exogenous introduction of
382 DNA in the cytosol by transfection, leakage of genomic DNA following DNA damage leads to

383 unconventional STING signalling, predominantly engaging NF-kB rather than IRF3 (Dunphy et al.,
384 2018). Our NER inflammatory activation skewed towards cytokines rather than interferon supports
385 the latter mechanism of STING engagement. Importantly, our work does not exclude the potential
386 involvement of other DNA sensors nor the role of additional mechanisms connecting nuclear
387 deformation and rupture to proinflammatory signalling in WASp null cells. Remarkably, the NER
388 inflammatory signature induced in confined WASp null macrophages has been linked to the
389 induction of senescence in fibroblasts (Sladitschek-Martens et al., 2022). Even if we have not
390 explored senescence in WASp null cells or tissues, the expression of this signature under
391 confinement, together with Lamin A/C defects and nuclear rupture, lead us to speculate that lack of
392 WASp may predispose to accelerated ageing of the myeloid compartment *in-vivo*. Moreover, these
393 findings suggest that inflammation may be connected to nuclear alterations in a broader group of
394 diseases referred to as actinopathies (Papa et al., 2021; Sprenkeler et al., 2021), underscoring the
395 relevance of investigating mechanical control of inflammation in immune cells. From a clinical
396 perspective, our study has implications for understanding the molecular basis of WAS autoimmunity.
397 Transcriptional data in human iPSCs-derived macrophages and total cells from the peripheral blood
398 of gene therapy-treated WAS patients consistently indicate that WASp restricts the accrual of
399 inflammation. However, inflammatory relapses are still frequent after treatment in WAS, including
400 following hematopoietic stem cell transplantation (Sudhakar et al., 2021). According to recent
401 evidence, including the data presented here, gene therapy may offer better control of inflammation
402 in treated patients (Sereni et al., 2019; Magnani et al., 2022). Nevertheless, providing a further
403 element to understand the origin of inflammation in WAS may help the management of residual
404 disease, especially for those patients who do not have access to gene therapy.
405 In summary, our results unveil a cell-intrinsic WASp-mediated mechanism to control nuclear
406 stability and inflammation under physiologically relevant settings, expanding the role of WASp-
407 driven Arp2/3 actin polymerization in preserving myeloid cell homeostasis in tissues.
408
409
410
411
412
413
414

415 # Materials and methods

416

417 ## Reagents and tools table

418

| Reagent/Resource | Reference or Source | Identifier |
|---|---|---|
| | | |
| **Experimental Models** | | |
| WASp$^{-/-}$ mice - B6.129S6-Wastm1Sbs/J | Jackson #:019458 | IMSR_JAX:019458 |
| HC and WAS PBMCs | San Raffaele Institute | Supplementary Table 5 |
| **Recombinant DNA** | | |
| pCDH-NLS-GFP | Addgene | #132772 |
| pMD2.G | Addgene | #12259 |
| psPAX2 | Addgene | #12260 |
| SEWW-eGFP-WASp | (Blundell et al., 2008) | / |
| **Antibodies Flow cytometry** | | |
| CD45 - APC-Cy7 | BioLegend | 103114 |
| CD11c - Bv786 | BioLegend | 117335 |
| F4/80 - Bv421 | eBioscience | 25-5870-80 |
| MHC-II - AF700R | BioLegend | 151507 |
| LY6C - PE | eBioscience | 11-0541-81 |
| CD64 - BV605 | BioLegend | 108923 |
| SiglecF - PerCP-Cy5.5 | BioLegend | 107105 |
| CD80 - APC | BioLegend | 139323 |
| CD86 - Bv650 | BioLegend | 104713 |
| CD3 - FITC | BioLegend | 100305 |
| LY6G - FITC | Bio-Rad | MCA6077GA |
| B220 - FITC | BioLegend | 103208 |
| CD19 - FITC | BioLegend | 115503 |
| NK1.1 - FITC | BioLegend | 116410 |
| **Antibodies FACS** | | |
| CD11c - Bv786 | BioLegend | 117308 |
| SiglecF - PerCP-Cy5.5 | BioLegend | 121406 |
| **Antibodies immunofluorescence** | | |
| Anti-Emerin | Thermo Fischer | PA5-29731 |
| Anti-H3K9me2 | Abcam | ab1220 |
| Anti-LMNA/C | Cell Signalling | mAb#4777 (4C11) |

| | | |
|---|---|---|
| Anti-γH2AX | Sigma Aldrich | 05-636 (JBW301) |
| Anti-Mouse-488, Donkey | Invitrogen | A21202 |
| Anti-Mouse-555, Goat | Invitrogen | A21424 |
| Anti-Mouse-647, Chicken | Invitrogen | A21463 |
| Anti-Rabbit-488, Goat | Invitrogen | A21441 |
| Anti-Rabbit-594, Donkey | Invitrogen | A21207 |
| **Antibodies western blot** | | |
| Anti-GAPDH-HRP | Sigma Aldrich | G9295 (GAPDH-71.1) |
| Anti-WASp | Santa Cruz Biotech | sc-13139 (B-9) |
| Anti-Lamin A/C | Cell Signalling | mAb#4777 (4C11) |
| Anti-STING | Cell Signalling | 13647 (D2P2F) |
| Anti-TUBα-HRP | Cell Signalling | #9099 (11H10) |
| Anti-mouse-HRP | Jackson | 115-035-003 |
| Anti-Rabbit-HRP | Jackson | 711-035-152 |
| **Chemicals, Enzymes and other reagents** | | |
| 2-mercaptoethanol | Gibco | 31350010 |
| ACK lysis buffer | Gibco | A1049201 |
| Alexa Fluor™ 555 Phalloidin | Thermo Fischer | A34055 |
| Alt-R® Cas9 Electroporation Enhancer | IDT | 1075916 |
| Alt-R® CRISPR-Cas9 tracrRNA | IDT | 1072533 |
| Alt-R® Negative Control crRNA #2 | IDT | 1072545 |
| Alt-R™ crRNA STING | IDT | Mm.Cas9.TMEM173.1.AA |
| Alt-R™ crRNA WASp | IDT | Mm.Cas9.WAS.1.AC |
| Alt-R™ spCas9 Nuclease V3 | IDT | 1081058 |
| Bovine Serum Albumine (BSA) | Sigma Aldrich | A8806 |
| Clarity ECL substrate | Bio-Rad | 170-5060 |
| Collagenase type 2 | Worthington | LS004176 |
| Counting Bright beads | Miltenyi | C36950 |
| DMXAA | Invivogen | tlrl-dmx |
| DNAse I from bovine pancreas | Millipore-Sigma | 11284932001 |
| EDTA | Thermo Fischer | 15575020 |
| FBS - low endotoxin | Euroclone | ECS0186D - lot. EUS037123 |
| Fibronectin Bovine protein | Thermo Fischer | 33010-018 |
| Gentamicin | Gibco | 15710064 |
| Glycine | Sigma Aldrich | G7126 |
| Hepes | Invitrogen | 15630080 |

| | | |
|---|---|---|
| Hoechst 33342 | Invitrogen | H3570 |
| IMDM medium | Thermo Fischer | 31980030 |
| Lenti-X concentrator | Takara | 631231 |
| Live and Dead staining –-Bv510 | Invitrogen | L34966 |
| LPS | Invivogen | tlrl-pb5lps |
| Mouse CD11c microbeads | Miltenyi | 130-125-835 |
| Mowiol 40-88 | Sigma Aldrich | 324590 |
| PDMS; SYLGARD 184 | Dow | 1673921 |
| PFA | Thermo Fischer | 28908 |
| Poly-Ethylene-Glycol (PEG) | Sigma Aldrich | 81260-1KG |
| PrimeScript™ RT Reagent Kit | Takara | RR036A |
| Protein inhibitor cocktail | Sigma Aldrich | P8340 |
| Recombinant mouse CCL19 (MIP3-β) | Gibco - Peprotech | 250-27B-1MG |
| Recombinant mouse MSC-F | Miltenyi | 130-101-706 |
| RIPA buffer | / | / |
| RNA Later™ | Invitrogen | AM7021 |
| RPMI 1640 medium | Thermo Fischer | 72400047 |
| Sodium Azide | Sigma Aldrich | 13412 |
| Sodium pyruvate | Gibco | 11360070 |
| Supernatant-containing GM-CSF | Produced by J558 cells | / |
| TB Green® Premix kit | Takara | RR420A |
| Triton-X-100 | Sigma Aldrich | X100-500ML |
| TRIzol™ reagent | Thermo Fischer | 15596026 |
| Tween-20 | Sigma Aldrich | 02286 |
| **Kits** | | |
| BCA assay kit | Thermo Fischer | 23225 |
| RNA high-sensitivity kit | Agilent | 5067-5579 |
| RNeasy micro kit | Qiagen | 74004 |
| Universal Index Twist kit 96 | Diatech-Labline | 101307 |
| WatchMaker - mRNA Library Prep Kit | Diatech-Labline | 7BK0001-024 |
| **Software** | | |
| Fiji (ImageJ) | v.1.54f | / |
| FlowJo | Tree Star, Inc. v.10.8.2 | / |
| Graphpad | Prism v.8.0.1 | / |
| R software | R version 4.3.1 | / |
| Biorender | www.biorender.com | |

| Other | | |
|---|---|---|
| J-558 cell line (GM-CSF producers) | / | / |

419

420

421

422 ## Methods and protocols

423

424 **Mice**

425 WASp$^{-/-}$ mice (IMSR_JAX:019458) on a C57BL/6 genetic background were a gift from S. Snapper
426 (Massachusetts General Hospital, Boston, Massachusetts, USA) (Snapper et al., 1998). Animal care
427 and experimentation were conducted under national and international laws and policies (Italian
428 D.L.gs. no. 26/2014 art.3.1A; European Directive 63/2010/UE). Mice were bred and maintained at
429 the ICGEB animal Bio-experimentation facility in sterile isolators (12h/12h light/dark cycle, T
430 21 °C ± 2 °C, RH 55% ± 10%) and received a standard chow diet and water *ad libitum*. Experiments
431 involving *ex-vivo* bone marrow culture were performed using WKO males' mice and WT littermates
432 as controls of 8-12 weeks of age. In case of *in-vivo* experiments WASp$^{-/-}$ and heterozygous WASp$^{+/-}$
433 female mice of 10 and 25 weeks of age were employed.

434

435 **Primary murine cell culture and human PBMCs**

436 Mouse BM-derived macrophages (BMDMs) were generated in vitro from BM of C57BL/6 WT or WKO
437 mice using recombinant M-CSF (rMCSF, Miltenyi Biotech). BM-derived cells were cultured at a
438 concentration of 1 × $10^6$ cells/mL in non-treated 10 cm Petri dishes (Greiner) for 7 days using RPMI
439 1640 supplemented with 20 ng/mL rMCSF, 10% low endotoxin FBS (Euroclone), plus 50 µg/mL
440 gentamicin (Gibco), 50 µM 2-mercaptoethanol (Gibco) and 1% Sodium Pyruvate (Gibco). Mouse BM-
441 derived DCs (BMDCs) were generated in vitro from bone marrow of C57BL/6 WT or WKO mice using
442 supernatant containing GM-CSF produced from J558 cell line. BMDCs were cultured at a
443 concentration of 1.5 × $10^6$ cells/mL in Nunc-nontreated 6 well-plates (Thermo Fisher Scientific) for 7
444 days using IMDM supplemented with 30% GM-CSF supernatant, 10% low endotoxin FBS (Euroclone),
445 50 µg/mL gentamicin (Gibco) and 50 µM 2-mercaptoethanol (Gibco). All mice used for BM culture
446 were males of 7 to 12 weeks of age.

447 Human PBMCs were gently provided by Dr. Anna Villa from San Raffaele Institute and shipped in
448 RNA Later™ (Thermo Fischer Scientific). RNA extraction and library preparation for sequencing are

449 described in the respective paragraphs. Information about patients is provided in Supplementary
450 Table 4.
451
452 **Flow cytometry and sorting of alveolar macrophages**
453 Alveolar macrophages (AMO) were obtained from homozygous WASp$^{-/-}$ or heterozygous WASp$^{+/-}$
454 female mice of 10 or 25 weeks old. After animal sacrifice, lungs were perfused in PBS to wash away
455 red blood cells and digested with collagenase type 2 (265 U/mL; Worthington) and DNase I
456 (250 U/mL; Millipore-Sigma) in complete media at 37°C for 30'. Collagenase activity was then
457 stopped by EDTA 10 mM, and cell suspension was filtered using 100 µm cell strainer (Corning). The
458 obtained single cell suspension was enriched for CD11c+ population using the mouse CD11c
459 microbeads (Miltenyi) and stained with anti-CD11c, anti-CD45 and anti-SiglecF. $5 \times 10^6$ cells/mL were
460 resuspended in PBS 2% FBS for sorting and at least 100.000 AMO were sorted with a BD FACSAria II
461 in PBS 20% FBS. Sorted AMO were centrifuged and frozen at -70°C in 350 µL of RLT lysis buffer prior
462 to RNA extraction. Flow cytometry analysis was performed in a BD FACSCelesta™ starting from 1/5
463 of single cell suspension before CD11c enrichment, using antibodies reported in Supplementary
464 Table 7 and Counting Bright beads (Miltenyi). All antibodies were incubated 1 h at 4°C in dark
465 conditions. After antibody staining, samples were incubated 20' at 4°C in dark conditions with Live
466 and Dead fixable aqua (Invitrogen) 1:1000 in PBS and fixed over-night in PBS 1% PFA before a final
467 wash and acquisition. Data analysis was performed on FlowJo software.
468
469 **RNA extraction and gene expression analysis**
470 RNA from BMDM at steady state was obtained using of TRIzol™ reagent (Thermo Fischer Scientific)
471 and treated with DNaseI before retro transcription. RNA extraction and purification of sorted AMO,
472 confined BMDM and human PBMCs was performed by RNeasy micro kit (Qiagen). Retro
473 transcription and qPCR were done by PrimeScript™ RT Reagent Kit (Takara) and TB Green® Premix
474 (Takara). Real time machine used for qPCR was a CFX96 Touch (Bio-Rad). Specific primers used for
475 amplification were the following (5'-> 3'):
476
477 <u>Mouse</u>: Gapdh fwd AGAAGGTGGTGAAGCAGGCAT, Gapdh rev CGAAGGTGGAAGAGTGGGAGT; Il6
478 fwd GAGGATACCACTCCCAACAGA, Il6 rev AAGTGCATCATCGTTGTTCAT.
479

480 Human: Hprt1 fwd AATTATGGACAGGACTGAACGTCTTGCT, rev
481 TCCAGCAGGTCAGCAAAGAATTTATAGC; Mxa fwd ACAGAACCGCCAAGTCCAAA, rev
482 GCGGATCAGCTTCTCACCTT; Rsad2 fwd ATCCTTTGTGCTGCCCCTTG, rev
483 TTGATCTTCTCCATACCAGCTTCC; Il6 fwd AGACAGCCACTCACCTCTTCAG, rev
484 TTCTGCCAGTGCCTCTTTGCTG; Il1b fwd ATGATGGCTTATTACAGTGGCAA, rev
485 GTCGGAGATTCGTAGCTGGA.
486
487 **Lentiviral preparation and BMDM infection**
488 Second generation lentiviral particles were prepared by co-transfecting HEK-293T cells with plasmid
489 of interest, relative packaging and envelope. 48 hours after transfection, supernatant-containing
490 virus was collected, centrifuged 300g for 5' to remove cell debris and filtered through 0.45 µm filter.
491 Cleared supernatants were mixed with Lenti-X concentrator (Takara) and concentrated 100x,
492 following manufacturer instructions. 20 µL of concentrated lentiviral particles were used to infect 2
493 x $10^6$ BMDM at day 4 in a 6-well plate. At day 6, viral-containing supernatant was removed and
494 attached cells were washed 2x in sterile PBS. Infected BMDM were used at day 7 after two more
495 washes in PBS to get rid of any remaining viral particle. Plasmid used for generation of lentivectors
496 were the following: pMD2.G (Addgene #12259), psPAX2 (Addgene #12260), SEWW-eGFP-WASp
497 (Blundell et al., 2008), pCDH-NLS-GFP (Addgene #132772), pTRIP-mCherry-FLAG-cGAS
498 E225A/D227A (Addgene #127657).
499
500 **CRISPR-Cas9 RNPs electroporation**
501 CRISPR-Cas9-mediated gene knock-out was achieved through electroporation of ribonucleoprotein
502 (RNP) particles containing crRNA, tracRNA and Cas9 protein complexes. spCas9 and RNA oligos were
503 purchased from IDT, annealed and mixed following manufacturer instructions. At day 4 of
504 differentiation, 1.5 x $10^6$ cells were electroporated in 100 µL of media in a NEPA electroporator with
505 the following parameters: poring pulse 275 V, 4 x 1 ms, interval 50 ms, D. Rate 10 %; transfer pulse
506 20 V, 5 x 50 ms, interval 50 ms, D. Rate 40 %, polarity +/-. After 24 h media was changed and cells
507 were used for experiments at day 7 of differentiation.
508
509 **6-well plate confiner**
510 Mechanical confinement was performed in 6-well plates (Liu et al., 2015). 12 mm glass coverslips
511 were washed with hand soap, rinsed in $ddH_2O$, then in isopropanol and dried with a pressurized air

512 gun. The clean coverslips were treated in a plasma cleaner (Diener Zepto) at 40W for 30 s. To make
513 pillars of desired height, polydimethylsiloxane (PDMS; SYLGARD 184, Dow) was mixed at a ratio of
514 PDMS A:cross-linker B 1:10 (wt/wt) and poured on top of wafer molds-containing pillars of 3 µm or
515 6 µm. The wafer molds, containing pillars of 3 µm or 6 µm, were fabricated by conventional
516 micromachining from square pieces (25x25 mm) of a 500 µm thick silicon wafer. After cleaning the
517 wafer with acetone and isopropanol, a positive photoresist MEGAPOSIT™ SPR™220 3.0 or 7.0 was
518 spinned on. After the soft bake, they were exposed to a UV lamp for 30 seconds with a suitable mask
519 and subjected a post-bake process. The development was carried out with MF24A. To functionalized
520 with micropillars, glass coverslips were pressed to the wafers and baked at 85°C for 20 min before
521 being carefully detached with a blade. After a wash in isopropanol, coverslips with micropillars were
522 dried and plasma treated for 30 more seconds. Finally, these coverslips were washed in PBS and
523 incubated with non-adhesive PEG solution (Sigma) 500 µg/mL in PBS for 30 min at RT and UV-
524 sterilized for 20'. Before confinement, functionalized glass coverslips were washed in $H_2O$ and PBS
525 and kept in sterile PBS at 4°C for a maximum of 48 h. To perform confinement experiments, we used
526 large PDMS pistons placed on the plate lid to press the coverslips on the bottom of the plate. A drop
527 of 250 µL containing 300.000 cells for immunofluorescent assays or 500.000 cells for RNA collection
528 was confined for each well. 6-well plates with a glass bottom were used for cell imaging (MatTek,
529 P06G-1.5-20-F); whereas non-treated 6-well plates (Corning) were adopted for RNA experiments.
530 Nuclear blebbing quantification was performed right after confinement on live cells based on
531 Hoechst 33342 staining (1:10.000 in PBS). Both types of confinements were kept for 1 h before
532 fixation or RNA extraction. Fixation for IF was performed directly on confined cells, by leaving 4%
533 PFA for 45 min before removing the lid, quenching PFA with 0,1 M glycine in PBS and washing cells
534 3x with PBS before proceeding with IF staining.
535
536 **Microchannel preparation and live imaging**
537 Microchannels MC004 were purchased from 4DCell. And prepared following manufactures
538 instructions. Coating was performed using 10 µg/mL fibronectin for 1 h at RT. Before utilization,
539 channels were incubated from 30 min to overnight in 2 mL of BMDM media. Timelapse imaging was
540 carried out overnight on a Nikon Eclipse TiE inverted microscope equipped with a 20x/0.75 NA dry
541 objective, a motorized stage and a humidified chamber at 37°C and 5% $CO_2$. Live imaging of migrating
542 macrophages in microchannels was recorded with a frame every 5 min, based on NLS-GFP (FITC
543 channel) and DIC (transmitted light). After overnight migration, cells inside channels were fixed by

544 adding 10 µL of 4% PFA to each accession port and waiting for 1 h at RT before washing in PBS.
545 Channels were kept in PBS 0,02% Sodium Azide until further imaging. Hoechst 1:1000 in PBS was
546 added for at least 1 h before imaging fixed microchannels to facilitate detection and segmentation
547 of nuclear morphology and herniations Fixed samples were imaged on a Zeiss LSM880 confocal
548 microscope with a 63x/1.4 NA oil objective for individual nuclei and a 20x/0.60 NA dry objective for
549 large field acquisitions and quantification of cell entry.
550
551 **Immunofluorescence imaging**
552 Immunofluorescence staining at steady state was done with 50.000 BMDM seeded on fibronectin-
553 coated (10 µg/mL, Millipore Sigma) 12 mm microscope slides (Epredia, Thickness value #1). Cells
554 were left 30' at 37°C and 5% $CO_2$ to adhere. Fixation was performed in 4% PFA for 7 min at RT,
555 followed by quenching in 0,1 M glycine in PBS for 3 min. After 3x washes in PBS, cells were
556 permeabilized in PBS 1% BSA, 0,1% Triton-X100, blocked in PBS 3% BSA, 10 mM Hepes and stained
557 ON at 4°C in primary antibodies diluted in PBS 0,2% BSA, 0,1% Triton-X100. Secondary antibodies
558 were incubated at RT for 2h, followed by eventual phalloidin staining (Thermo Fischer Scientific, used
559 1:500) and 10 min nuclear staining with Hoechst 33342 (Invitrogen) 1:1000 in PBS. Slides were
560 mounted with Mowiol and imaged at Zeiss LSM880 confocal microscope with a 63x/1.4 NA oil
561 objective, or a 20x/0.60 NA dry objective. A full list of antibodies, dyes and probes used is presented
562 in supplementary table 7.
563
564 **AFM based indentation measurements**

565 AFM-based indentation measurements were performed by NanoWizard III AFM (JPK Instruments,
566 Bruker) integrated with an inverted optical microscope (Axiovert 200; Zeiss) for sample observation.
567 Cells were analysed in petri-dish and in culture medium at room temperature. The status of cells
568 was constantly monitored by optical microscope. Indentation of the whole cell body was performed
569 using MLCT-SPH-5um probes (Bruker), which have a cylindrical tip shank ending in a spherical tip
570 with a 5 µm radius and a nominal spring constant of 0.06 N/m. Once localized the cell by optical
571 microscope, the probe was brought over the nucleus area and pressed down to indent the cell. The
572 motion of the z-piezo and the force were recorded. On each cell three to five force–displacement (F-
573 D) curves were acquired with a force load of 0.5-1nN and at a rate of at 5µm/s in closed-loop
574 feedback mode. Cell elastic properties were assessed by determining the Young's modulus (E), which
575 can be evaluated by fitting the force (F) indentation ($\delta$) curves with the Hertz model.

576

577 $$F = \frac{4}{3}\frac{E}{(1-\nu^2)}\sqrt{R}\delta^{3/2}$$

578

579 where F is the force, R is the radius of the spherical indenter and ν is the sample's Poisson ratio (set
580 to 0.5 for the cell) and δ is the indentation depth.
581 Data fitting was performed on the approaching F–D curves. JPK Data Processing software was used
582 to convert the F-D curves into the force–indentation curves by subtracting the cantilever bending
583 from the signal height to calculate indentation. The resulting force-indentation curves were fitted
584 with the Hertz model for indentation depth of 500 nm.

585

586 **Transwell migration assay**

587 24-well plates bearing transwell inserts of 5 µm and 3 µm. 5 µm plates were from Corning; 3 µm
588 plates from Thermo Fischer Scientific. At day 7 of differentiation, cells were detached using MACS
589 buffer (0,5% BSA, 2 mM EDTA in PBS), counted and resuspended in media without FBS containing
590 200 ng/mL of LPS (Invivogen) for 30 min in incubator. After LPS washout, cells were plated at a
591 concentration of 200.000 cells in 200 µL for each insert in complete media. On the bottom of each
592 well, 600 µL of complete media supplemented with 250 ng/mL of CCL19 (Peprotech) as
593 chemoattractant were added to promote transmigration. Cells were kept 5 h in incubator to allow
594 migration, following by collection of migrated cells for flow cytometry or IF analysis. Flow cytometry
595 quantification of migrating cells was performed at BD Accuri™ C6 flow cytometer, using Counting
596 Bright beads and normalizing the number of transmigrating cells to the total number of plated cells.

597

598 **Protein extraction and western blot**

599 Cells were lysed in an appropriated volume of RIPA buffer (50 mM Tris/HCl pH 7.5, 150 mM NaCl, 1%
600 NP-40, 0,1% SDS, 0,1% DOC in $ddH_2O$) supplemented 1:30 with protease inhibitor cocktail (Sigma
601 P8340). After centrifugation at 17000 g for 20 min, supernatant-containing protein extracts were
602 kept at -20°C until further processing. Total protein concentration was quantified by means of BCA
603 assay (Thermo Fisher), following manufacturer instructions. At least 20 µg of total protein lysates
604 were loaded on a 10% custom made polyacrylamide gel and transferred on PVDF membranes upon
605 SDS-page electrophoresis. Membranes were blocked at least 1 h at RT in 1x TBS, 0,1% Tween 20
606 (TBST), 3% dry fat milk. Primary antibodies were incubated ON at 4°C on a shaker. After 3x washes
607 in TBST, secondary HRP-conjugated antibodies were kept 1-2 h at RT. Chemiluminescence signal was

608 developed by Clarity ECL substrate (Bio-Rad) on a ChemiDoc™ Touch (Bio-Rad). A list of antibodies
609 used is reported in supplementary table 7.
610
611 **Library preparation and RNA-sequencing**
612 For mouse and human samples, total RNA was extracted using RNeasy Micro kit (Qiagen), according
613 to the manufacturer's protocol. RNA purity, integrity and quantity was checked at TapeStation 2200
614 (Agilent Technologies Inc., Santa Clara, CA, USA). RNA-seq libraries were prepared from 3 ng (human
615 PBMCs) or 5 ng (mouse BMDM) of total RNA using mRNA Library Prep Kit (WATCHMAKER) following
616 manufacture instruction. Briefly, we selected poly(A) using magnetic beads to focus sequencing on
617 polyadenylated transcripts. After RNA fragmentation, a step of cDNA synthesis was performed. The
618 resulting fragments were used for A-tailing and were ligated to the adapters and Index Anchors
619 (TWIST bioscience, Twist universal system). PCR amplification (21 cycles) was performed to generate
620 the final indexed cDNA libraries. Individual library quantification and quality assessment was
621 performed using TapeStation 2200. Libraries were sent to Macrogen to be sequences on Novaseq
622 (Human PBMCs) or NovaseqX (Mouse BMDM) instrument on Illumina platform as paired end run
623 150 bp reads. A total of 6 PBMCs samples were sequenced before as well after gene therapy. Four
624 biological replicates of BMDM confined per genotype and three replicates for unconfined control
625 were sequenced.
626
627 **RNA-sequencing analysis**
628 Raw FastQ files were downloaded from Macrogen. Quality control, trimming and alignment were
629 performed using standard pipelines for FastQC, Trimgalore and STAR.
630 Confiner data: Raw reads count matrix outputs were imported and analysed in R software (R version
631 4.3.1). Normalized reads were obtained by standard DEseq2 functions and used for heatmaps
632 visualization. DESeq2 package (Love et al., 2014) was further used for differential gene expression
633 analysis. GSEA was performed on gseGO function of ClusterProfiler package on Log2FC ordered
634 genes with p-value cutoff of 0.01 and Benjamini-Hochberg p-value correction. DEGs were considered
635 as genes bearing p-value< 0.05 and a Log2FC> 1.2 or Log2FC< -1.2. GO analysis was performed on
636 DEGs using enrichGO function, based on biological processes, with a p-value cutoff of 0.05 and
637 Benjamini-Hochberg statistical correction. Visualizations of functional enrichment results were
638 obtained by ClusterProfiler and ggplot2 packages.

639 PBMCs data: DESeq2 analysis was performed starting on unnormalized reads comparing WAS pre-
640 vs post-gene therapy samples. gseGO from ClusterProfiler have been used to perform GSEA on
641 Log2FC ordered genes, using Entrez ID as key type, "BP" as ontology and 0.05 as p-value cutoff,
642 without further statistical correction methods. Full list of GSEA is available as Supplementary Table
643 6.
644 Analysis of publicly available dataset from GSE107963: Data were downloaded as TPM normalized
645 count matrix from GSE107963 (www.ncbi.nlm.nih.gov/geo/download/?acc=GSE107963, data
646 deposited on 15.12.2022 and downloaded on 13.08.2024). Samples used for analysis refer to 3 WAS
647 iPSCs (WASp -) and 3 isogenic iPSCs corrected to re-express WASp (WASp +), both differentiated into
648 macrophages. TPM matrix was filtered and further processed to keep only genes with non-zero
649 reads. Log2(TPM+1) was used for heatmap visualization.
650
651 **Image analysis**
652 All raw images were analysed in Fiji ImageJ (Schindelin et al., 2012), using custom-written macros.
653 Lamin A/C alteration: Lamin A/C alteration score has been calculated based on standard deviation
654 (σ) of Lamin A/C signal. Nuclear segmentation has been based on Hoechst 33342 channel of z-
655 projected nuclei, with a size threshold > 10 $\mu m^2$, to exclude potential micronuclei from the analysis.
656 Alteration score has been plotted as σ/10. Masks of Lamin A/C wrinkles for representative pictures
657 has been obtained by an adaptive threshold method.
658 Chromocenters and H3K9me2 quantification: to quantify the number of chromocenters and the area
659 of peripheral heterochromatin, nuclei were first segmented based on Hoechst 33342 signal.
660 Chromocenters were detected based on an adaptive threshold and a size cutoff. Area of peripheral
661 heterochromatin has been calculated as the sum of chromocenters' area in close proximity to
662 nuclear edges, as those within 1 µm from nuclear borders. The same cutoff has been used for
663 H3K9me2 peripheral heterochromatin, measuring fluorescent intensity instead of chromocenters
664 area.
665 Microchannels analysis and WASp-GFP distribution: quantification of cells inside microchannels an
666 nuclear rupture events have been conducted manually. Kymographs of NLS-GFP migrating cells were
667 generated using a semi-automated macro in ImageJ. WASp-GFP distribution has been obtained in a
668 semi-automated way as follow. Briefly individually cropped cells inside channels were subjected to
669 automatic nuclear detection. Nuclear centre of mass was then moved to the centre of the image and
670 all individual cells were cropped and horizontally aligned. The size of the cells was normalized at 600

pixels and expanded 50 times before saving at a resolution size of 1200x200 pixels (w x h). Size normalized cells were then merged by Stack>Z project>Average Intensity to obtain an average intensity map profile of WASp distribution.

**Statistics**

Primary data were collected in Microsoft Excel and statistical analyses were performed using GraphPad Prism version 8. For comparison between two or more groups with normally distributed data two-tailed Student's t-test, one-way ANOVA or two-way ANOVA were used as appropriate. The non-parametric Kruskal-Walli's test with Dunn's multiple comparison was performed to compare three or more unmatched groups. In case of normalized values to 1 or 0, statistics has been calculated by a one-sample t-test. *P* values <= 0.05 were considered significant and marked by asterisk, if not stated differently.

## Supplementary information

Description of supplementary data

- Supplementary table 1: RNA-seq data normalized reads BMDM
- Supplementary table 2: Gene lists for signatures used in Fig.5
- Supplementary table 3: Gene list of inflammatory signatures used in Fig.6
- Supplementary table 4: WAS patients' information
- Supplementary table 5: RNA-seq data normalized reads PBMCs
- Supplementary Table 6: GSEA on WAS PBMCs dataset
- Supplementary table 7: List of antibodies used in the work

## Data availability

Sequencing data have been deposited at GEO database: BMDM confiner data (accession: GSE285024), publicly available as of the 24/12/2024 and PBMCs WAS data (accession: GSE285174), publicly available as of the 25/12/2024. Source data are provided in supplementary files. Any additional information required to reanalyse the data reported in this paper is available from the lead contact upon formal request.

## Author contributions

**R.A**, **G.M.P** and **F.B** conceived the study and designed the experiments. **R.A** performed most of the experiments, data analysis, and prepared the figures. **R.A** and **F.B** wrote the manuscript. **G.B** helped in the execution of experiments and performed WASp-GFP confinement. **Z.A** provided training and support for the confiner assays and helped in performing confiner experiments in Fig.3 (A, B and C). **M.M** assisted in image analysis. **G.M.P** and **L.L.R** assisted in the experimental part and critical discussion of the data. **G.M.P** prepared library for sequencing. **M.C** prepared photolithographic molds used for confiner slides fabrication. **L.A** performed and analysed atomic force microscopy. **M.C.C**, **F.F**, **A.A** and **A.V** provided human PBMCs samples. **A.-M.L.-D** critically discussed the data and the manuscript. **F.B** supervised the whole study. All authors read and approved the final version of the manuscript.

## Disclosure and competing interest's statement

The authors declare no competing interests.

## Acknowledgements

This work was supported by Telethon grant GGP20102 to **F.B**. **G.B**, **G.M.P** and **L.L.R**- were supported by ICGEB Arturo Falaschi pre- and post-doctoral fellowships. **R.A** was supported by Italian Telethon. **R.A** received an EMBO scientific exchange grant (10017) to perform part of the work in the lab of **A.-M.L.-D**. We Thank Luca Triboli from ICGEB Trieste to help discussing bioinformatic data analysis.

735 ## References


736 Ablasser, A., and Gulen, M. F. (2016). The role of cGAS in innate immunity and beyond. *J. Mol. Med.* 94,
737 1085–1093. doi:10.1007/s00109-016-1423-2.

738 Alraies, Z., Rivera, C. A., Delgado, M. G., Sanséau, D., Maurin, M., Amadio, R., et al. (2024). Cell shape
739 sensing licenses dendritic cells for homeostatic migration to lymph nodes. *Nat. Immunol.* 25.
740 doi:10.1038/S41590-024-01856-3.

741 Amadio, R., Piperno, G. M., and Benvenuti, F. (2021). Self-DNA Sensing by cGAS-STING and TLR9 in
742 Autoimmunity : Is the Cytoskeleton in Control ? *Front. Immunol.* 12. doi:10.3389/fimmu.2021.657344.

743 Bastianello, G., Porcella, G., Beznoussenko, G. V., Kidiyoor, G., Ascione, F., Li, Q., et al. (2023). Cell stretching
744 activates an ATM mechano-transduction pathway that remodels cytoskeleton and chromatin. *Cell*
745 *Rep.* 42, 113555. doi:10.1016/j.celrep.2023.113555.

746 Bell, E. S., Shah, P., Zuela-Sopilniak, N., Kim, D., Varlet, A.-A. A., Morival, J. L. P. P., et al. (2022). Low lamin A
747 levels enhance confined cell migration and metastatic capacity in breast cancer. *Oncogene* 41, 1–20.
748 doi:10.1038/S41388-022-02420-9.

749 Blundell, M. P., Bouma, G., Calle, Y., Jones, G. E., Kinnon, C., and Thrasher, A. J. (2008). Improvement of
750 Migratory Defects in a Murine Model of Wiskott–Aldrich Syndrome Gene Therapy. *Mol. Ther.* 16, 836–
751 844. doi:10.1038/MT.2008.43.

752 Blundell, M. P., Worth, A., Bouma, G., and Thrasher, A. J. (2010). The Wiskott-Aldrich syndrome: The actin
753 cytoskeleton and immune cell function. *Dis. Markers* 29, 157–175. doi:10.3233/DMA-2010-0735.

754 Calixto Vieira, R., Goncalves, L., Westerberg, L. S., Rhaissa, C., Vieira, C., and Goncalves Pinho, L. (2023).
755 Understanding immunoactinopathies: A decade of research on WAS gene defects. *Pediatr. Allergy*
756 *Immunol.* 34, e13951. doi:10.1111/PAI.13951.

757 Caridi, C. P., Plessner, M., Grosse, R., and Chiolo, I. (2019). Nuclear actin filaments in DNA repair dynamics.
758 *Nat. Cell Biol. 2019 219* 21, 1068–1077. doi:10.1038/s41556-019-0379-1.

759 Cervantes-Luevano, K. E., Caronni, N., Castiello, M. C., Fontana, E., Piperno, G. M., Naseem, A., et al. (2018).
760 Neutrophils drive type I interferon production and autoantibodies in patients with Wiskott-Aldrich
761 syndrome. *J. Allergy Clin. Immunol.* 142, 1605-1617.e4. doi:10.1016/j.jaci.2017.11.063.

762 Chen, N. Y., Kim, P. H., Tu, Y., Yang, Y., Heizer, P. J., Young, S. G., et al. (2021). Increased expression of LAP2β
763 eliminates nuclear membrane ruptures in nuclear lamin–deficient neurons and fibroblasts. *Proc. Natl.*
764 *Acad. Sci. U. S. A.* 118, 1–9. doi:10.1073/pnas.2107770118.

765 Davidson, P. M., Denais, C., Bakshi, M. C., and Lammerding, J. (2014). Nuclear deformability constitutes a
766 rate-limiting step during cell migration in 3-D environments. *Cell. Mol. Bioeng.* 7, 293.
767 doi:10.1007/S12195-014-0342-Y.

768 De Silva, N. S., Siewiera, J., Alkhoury, C., Nader, G. P. F., Nadalin, F., de Azevedo, K., et al. (2023). Nuclear
769 envelope disruption triggers hallmarks of aging in lung alveolar macrophages. *Nat. Aging* 3, 1251–

1268. doi:10.1038/s43587-023-00488-w.

Decout, A., Katz, J. D., Venkatraman, S., and Ablasser, A. (2021). The cGAS–STING pathway as a therapeutic target in inflammatory diseases. *Nat. Rev. Immunol.* doi:10.1038/s41577-021-00524-z.

Delgado, M.-G., Burkhart, A.-K., Villar, J., Amadio, R., Racz, V. S., Sanséau, D., et al. (2024). The Arp2/3 complex maintains genome integrity and survival of epidermal Langerhans cells. *bioRxiv*. Available at: https://doi.org/10.1101/2024.12.27.630538.

Denais, C. M., Gilbert, R. M., Isermann, P., McGregor, A. L., Te Lindert, M., Weigelin, B., et al. (2016). Nuclear envelope rupture and repair during cancer cell migration. *Science (80-. ).* 352. Available at: /pmc/articles/PMC4833568/ [Accessed March 24, 2023].

Dou, Z., Ghosh, K., Vizioli, M. G., Zhu, J., Sen, P., Wangensteen, K. J., et al. (2017). Cytoplasmic chromatin triggers inflammation in senescence and cancer. *Nature* 550. doi:10.1038/nature24050.

Du, H., Bartleson, J. M., Butenko, S., Alonso, V., Liu, W. F., Winer, D. A., et al. (2022). Tuning immunity through tissue mechanotransduction. *Nat. Rev. Immunol.* 23, 174. doi:10.1038/S41577-022-00761-W.

Dunphy, G., Flannery, S. M., Almine, J. F., Connolly, D. J., Paulus, C., Jønsson, K. L., et al. (2018). Non-canonical Activation of the DNA Sensing Adaptor STING by ATM and IFI16 Mediates NF-κB Signaling after Nuclear DNA Damage. *Mol. Cell*. doi:10.1016/j.molcel.2018.07.034.

En, A., Bogireddi, H., Thomas, B., Stutzman, A. V., Ikegami, S., LaForest, B., et al. (2024). Pervasive nuclear envelope ruptures precede ECM signaling and disease onset without activating cGAS-STING in Lamin-cardiomyopathy mice. *Cell Rep.* 43, 114284. doi:10.1016/j.celrep.2024.114284.

Gaertner, F., Reis-Rodrigues, P., de Vries, I., Hons, M., Aguilera, J., Riedl, M., et al. (2022). WASp triggers mechanosensitive actin patches to facilitate immune cell migration in dense tissues. *Dev. Cell* 57, 47-62.e9. doi:10.1016/j.devcel.2021.11.024.

Harada, T., Swift, J., Irianto, J., Shin, J. W., Spinler, K. R., Athirasala, A., et al. (2014). Nuclear lamin stiffness is a barrier to 3D migration, but softness can limit survival. *J. Cell Biol.* 204, 669. doi:10.1083/JCB.201308029.

Härtlova, A., Erttmann, S. F., Raffi, F. A. M., Schmalz, A. M., Resch, U., Anugula, S., et al. (2015). DNA Damage Primes the Type I Interferon System via the Cytosolic DNA Sensor STING to Promote Anti-Microbial Innate Immunity. *Immunity* 42, 332–343. doi:10.1016/j.immuni.2015.01.012.

Jain, N., and Vogel, V. (2018). Spatial confinement downsizes the inflammatory response of macrophages. *Nat. Mater.* 17, 1134–1144. doi:10.1038/s41563-018-0190-6.

Kim, J. K., Louhghalam, A., Lee, G., Schafer, B. W., Wirtz, D., and Kim, D. H. (2017). Nuclear lamin A/C harnesses the perinuclear apical actin cables to protect nuclear morphology. *Nat. Commun. 2017 81* 8, 1–13. doi:10.1038/s41467-017-02217-5.

Kovacs, M. T., Vallette, M., Wiertsema, P., Dingli, F., Loew, D., Nader, G. P. de F., et al. (2023). DNA damage induces nuclear envelope rupture through ATR-mediated phosphorylation of lamin A/C. *Mol. Cell* 83,

805 3659. doi:10.1016/J.MOLCEL.2023.09.023.
806 Lavenus, S. B., Vosatka, K. W., Caruso, A. P., Ullo, M. F., Khan, A., and Logue, J. S. (2022). Emerin regulation
807 of nuclear stiffness is required for fast amoeboid migration in confined environments. *J. Cell Sci.* 135.
808 doi:10.1242/JCS.259493/VIDEO-5.
809 Le, H. Q., Ghatak, S., Yeung, C. Y. C., Tellkamp, F., Günschmann, C., Dieterich, C., et al. (2016). Mechanical
810 regulation of transcription controls Polycomb-mediated gene silencing during lineage commitment.
811 *Nat. Cell Biol.* 18, 864–875. doi:10.1038/ncb3387.
812 Lee, P. P., Lobato-Márquez, D., Pramanik, N., Sirianni, A., Daza-Cajigal, V., Rivers, E., et al. (2017). Wiskott-
813 Aldrich syndrome protein regulates autophagy and inflammasome activity in innate immune cells.
814 *Nat. Commun.* 8, 1–13. doi:10.1038/s41467-017-01676-0.
815 Linder, S., Nelson, D., Weiss, M., and Aepfelbacher, M. (1999). Wiskott-Aldrich syndrome protein regulates
816 podosomes in primary human macrophages. *Cell Biol. Commun. by John A. Glomset* 96, 9648–9653.
817 Available at: www.pnas.org. [Accessed March 9, 2022].
818 Liu, Y. J., Le Berre, M., Lautenschlaeger, F., Maiuri, P., Callan-Jones, A., Heuzé, M., et al. (2015).
819 Confinement and low adhesion induce fast amoeboid migration of slow mesenchymal cells. *Cell* 160,
820 659–672. doi:10.1016/j.cell.2015.01.007.
821 Love, M. I., Huber, W., and Anders, S. (2014). Moderated estimation of fold change and dispersion for RNA-
822 seq data with DESeq2. *Genome Biol.* 15, 1–21. doi:10.1186/s13059-014-0550-8.
823 Magnani, A., Semeraro, M., Adam, F., Booth, C., Dupré, L., Morris, E. C., et al. (2022). Long-term safety and
824 efficacy of lentiviral hematopoietic stem/progenitor cell gene therapy for Wiskott-Aldrich syndrome.
825 *Nat. Med.* 28. doi:10.1038/s41591-021-01641-x.
826 Mu, X., Tseng, C., Hambright, W. S., Matre, P., Lin, C. Y., Chanda, P., et al. (2020). Cytoskeleton stiffness
827 regulates cellular senescence and innate immune response in Hutchinson–Gilford Progeria Syndrome.
828 *Aging Cell* 19, 1–16. doi:10.1111/acel.13152.
829 Mukherjee, S., Abdisalaam, S., Bhattacharya, S., Srinivasan, K., Sinha, D., and Asaithamby, A. (2019).
830 "Mechanistic link between DNA damage sensing, repairing and signaling factors and immune
831 signaling," in *Advances in Protein Chemistry and Structural Biology* (Academic Press Inc.), 297–324.
832 doi:10.1016/bs.apcsb.2018.11.004.
833 Nader, G. P. de F., Agüera-Gonzalez, S., Routet, F., Gratia, M., Maurin, M., Cancila, V., et al. (2021a).
834 Compromised nuclear envelope integrity drives TREX1-dependent DNA damage and tumor cell
835 invasion. *Cell* 184, 5230-5246.e22. doi:10.1016/J.CELL.2021.08.035.
836 Nader, G. P. de F., Williart, A., and Piel, M. (2021b). Nuclear deformations, from signaling to perturbation
837 and damage. *Curr. Opin. Cell Biol.* 72, 137–145. doi:10.1016/J.CEB.2021.07.008.
838 Naseem, A., Steinberg, Z., and Cavazza, A. (2022). Genome editing for primary immunodeficiencies: A
839 therapeutic perspective on Wiskott-Aldrich syndrome. *Front. Immunol.* 0, 4553.

840 doi:10.3389/FIMMU.2022.966084.
841 Nava, M. M., Miroshnikova, Y. A., Biggs, L. C., Whitefield, D. B., Metge, F., Boucas, J., et al. (2020).
842 Heterochromatin-Driven Nuclear Softening Protects the Genome against Mechanical Stress-Induced
843 Damage. *Cell* 181, 800. doi:10.1016/J.CELL.2020.03.052.
844 Oliveira, M. M. S., Kung, S. Y., Moreau, H. D., Maurin, M., Record, J., Sanséau, D., et al. (2022). The WASp
845 L272P gain-of-function mutation alters dendritic cell coordination of actin dynamics for migration and
846 adhesion. *J. Leukoc. Biol.* 111, 793–803. doi:10.1002/JLB.1AB0821-013RR.
847 Papa, R., Penco, F., Volpi, S., and Gattorno, M. (2021). Actin Remodeling Defects Leading to
848 Autoinflammation and Immune Dysregulation. *Front. Immunol.* 11, 1–11.
849 doi:10.3389/fimmu.2020.604206.
850 Patteson, A. E., Vahabikashi, A., Pogoda, K., Adam, S. A., Mandal, K., Kittisopikul, M., et al. (2019). Vimentin
851 protects cells against nuclear rupture and DNA damage during migration. *J. Cell Biol.* 218, 4079–4092.
852 doi:10.1083/JCB.201902046.
853 Piperno, G. M., Naseem, A., Silvestrelli, G., Amadio, R., Caronni, N., Cervantes-Luevano, K. E., et al. (2020).
854 Wiskott-Aldrich syndrome protein restricts cGAS/STING activation by dsDNA immune complexes. *JCI*
855 *Insight* 5. doi:10.1172/jci.insight.132857.
856 Prete, F., Catucci, M., Labrada, M., Gobessi, S., Castiello, M. C., Bonomi, E., et al. (2013). Wiskott-Aldrich
857 syndrome protein-mediated actin dynamics control type-I interferon production in plasmacytoid
858 dendritic cells. *J. Exp. Med.* 210, 355–374. doi:10.1084/jem.20120363.
859 Raab, M., Gentili, M., De Belly, H., Thiam, H. R., Vargas, P., Jimenez, A. J., et al. (2016). ESCRT III repairs
860 nuclear envelope ruptures during cell migration to limit DNA damage and cell death. *Science (80-. ).*
861 352, 359–362. doi:10.1126/science.aad7611.
862 Reis-rodrigues, P., Canigova, N., Avellaneda, M. J., Gaertner, F., Vaahtomeri, K., Riedl, M., et al. (2024).
863 Global coordination of protrusive forces in migrating immune cells. *bioRxiv*.
864 Schindelin, J., Arganda-Carreras, I., Frise, E., Kaynig, V., Longair, M., Pietzsch, T., et al. (2012). Fiji: An open-
865 source platform for biological-image analysis. *Nat. Methods* 9, 676–682. doi:10.1038/nmeth.2019.
866 Sereni, L., Castiello, M. C., Di Silvestre, D., Della Valle, P., Brombin, C., Ferrua, F., et al. (2019). Lentiviral
867 gene therapy corrects platelet phenotype and function in patients with Wiskott-Aldrich syndrome. *J.*
868 *Allergy Clin. Immunol.* 144, 825–838. doi:10.1016/j.jaci.2019.03.012.
869 Sereni, L., Castiello, M. C., Marangoni, F., Anselmo, A., di Silvestre, D., Motta, S., et al. (2018). Autonomous
870 role of Wiskott-Aldrich syndrome platelet deficiency in inducing autoimmunity and inflammation. *J.*
871 *Allergy Clin. Immunol.* 142, 1272–1284. doi:10.1016/j.jaci.2017.12.1000.
872 Shen, C., Postat, J., Cerf, A., Merino, M., Bhagrath, A., Patel, D., et al. (2024). DOCK8 regulates a
873 mechanosensitive actin redistribution that maintains immune cell cohesion and protects the nucleus
874 during migration. *bioRxiv*, 2024.07.26.605273. Available at:

875 https://www.biorxiv.org/content/10.1101/2024.07.26.605273v1%0Ahttps://www.biorxiv.org/content
876 /10.1101/2024.07.26.605273v1.abstract.
877 Sladitschek-Martens, H. L., Guarnieri, A., Brumana, G., Zanconato, F., Battilana, G., Xiccato, R. L., et al.
878 (2022). YAP/TAZ activity in stromal cells prevents ageing by controlling cGAS–STING. *Nature* 607, 790–
879 798. doi:10.1038/s41586-022-04924-6.
880 Snapper, S. B., Rosen, F. S., Mizoguchi, E., Cohen, P., Khan, W., Liu, C. H., et al. (1998). Wiskoff-Aldrich
881 syndrome protein-deficient mice reveal a role for WASP in T but not B cell activation. *Immunity* 9, 81–
882 91. doi:10.1016/S1074-7613(00)80590-7.
883 Song, X., Aw, J. T. M., Ma, F., Cheung, M. F., Leung, D., and Herrup, K. (2021). DNA repair inhibition leads to
884 active export of repetitive sequences to the cytoplasm triggering an inflammatory response. *J.*
885 *Neurosci.* 41, 9286–9307. doi:10.1523/JNEUROSCI.0845-21.2021.
886 Sprenkeler, E. G. G., Webbers, S. D. S., and Kuijpers, T. W. (2021). When Actin is Not Actin' like It Should: A
887 New Category of Distinct Primary Immunodeficiency Disorders. *J. Innate Immun.* 13, 3–25.
888 doi:10.1159/000509717.
889 Sudhakar, M., Rikhi, R., Loganathan, S. K., Suri, D., and Singh, S. (2021). Autoimmunity in wiskott–aldrich
890 syndrome: Updated perspectives. *Appl. Clin. Genet.* 14, 363–388. doi:10.2147/TACG.S213920.
891 Tang, W., Chen, X., Wang, X., Zhu, M., Shan, G., Wang, T., et al. (2023). Indentation induces instantaneous
892 nuclear stiffening and unfolding of nuclear envelope wrinkles. *Proc. Natl. Acad. Sci. U. S. A.* 120,
893 e2307356120. Available at: https://www.pnas.org/doi/abs/10.1073/pnas.2307356120 [Accessed
894 November 7, 2023].
895 Thiam, H. R., Vargas, P., Carpi, N., Crespo, C. L., Raab, M., Terriac, E., et al. (2016). Perinuclear Arp2/3-driven
896 actin polymerization enables nuclear deformation to facilitate cell migration through complex
897 environments. *Nat. Commun.* 7, 1–14. doi:10.1038/ncomms10997.
898 Vargas, P., Chabaud, M., Thiam, H. R., Lankar, D., Piel, M., and Lennon-Dumenil, A. M. (2016). Study of
899 dendritic cell migration using micro-fabrication. *J. Immunol. Methods* 432, 30–34.
900 doi:10.1016/J.JIM.2015.12.005.
901 Yuan, B., Zhou, X., Suzuki, K., Ramos-Mandujano, G., Wang, M., Tehseen, M., et al. (2022). Wiskott-Aldrich
902 syndrome protein forms nuclear condensates and regulates alternative splicing. *Nat. Commun. 2022*
903 *131* 13, 1–20. doi:10.1038/s41467-022-31220-8.
904
905
906
907
908
909

910
911
912
913
914 ## Figures and figure legends
915
916 **Figure 1 – Nuclear parameters are modified in WASp null macrophages**. (**A**) WT and WKO BMDM
917 were plated on glass and labelled with Hoechst to visualise nuclei. Representative images show
918 examples of the three parameters analysed: area (top), roundness (middle) and micronuclei
919 (bottom). Scale bar 10 µm. (**B**) Quantification of the three nuclear parameters depicted in A, each
920 dot is an independent experiment (*N*=6 experiments with *n*>2000 nuclei analysed for each
921 genotype). Two-tailed unpaired t-test; **P*<=0.05. (**C**) Representatives immunoblot (top left) and
922 relative quantification of LMNA/C protein expression relative to GAPDH (top right); *n*=3 biological
923 replicates. Data were analysed by one sample t-test. **P*<=0.05. (**D**) Expression of lamin isoforms from
924 RNA-seq analysis of WT and WKO BMDM. Normalized reads for Lmna, Lmnb isoforms 1 and 2 and
925 Emerin. Representative data from *n*=2 replicates. Data were analysed by two-way ANOVA test with
926 multiple comparisons and Sidak's correction method. *****P*<=0.0001. (**E**) Representatives maximum
927 z-projection of Lamin A/C staining (top) and the corresponding segmentation mask for wrinkles
928 detection (bottom). Quantification of Lamin A/C alterations as defined in methods. A higher score
929 indicates less homogeneity and more wrinkles. *n*=402 WT and *n*=302 WKO individual nuclei
930 measured, in 3 independent experiments. Scale bar 5 µm. Two-tailed unpaired t-test, **** =
931 *P*<0.0001. (**F**) Representative images of Lamin A/C (grey) and Emerin (red) co-staining (top) and line
932 intensity profiles (bottom). Histograms depict areas of colocalization at nuclear boundaries (blue
933 area) and in nuclear wrinkles (red area). Three independent co-labelling experiments were
934 performed. Scale bar 5 µm.
935
936
937 **Supplementary Figure 1 – Chromatin features and cellular mechanics in WT and WASp KO**
938 **macrophages**. (**A**) Representative images (left) and quantification (right) of the number of
939 chromocenters (heterochromatin foci) in WT and WKO BMDM nuclei and the mean area of
940 peripheral heterochromatin foci. *n*=65 individual nuclei measured from *N*=3 independent
941 experiments. Scale bar 5 µm. Statistics was calculated by two-tailed unpaired t-test. ns, not
942 significant. (**B**) Representative images (left) and quantification (right) of mean fluorescent intensity

943 and ratio of peripheral vs central H3K9me2 marker of facultative heterochromatin. *N*=3 independent
944 experiments, with *n*=65 individual nuclei measured in total. Data were analysed by two-tailed
945 unpaired t-test. ***$P$<=0.001; ns, not significant. Scale bar 5 µm. (**C**) Scheme of AFM-indentation
946 measurement of a single BMDM cell. Bright field image scale bar 50 µm (**D**) Quantification of Young's
947 modulus of *n*=71 WT and *n*=62 WKO BMDM cells, from three independent measurements. Data
948 were analysed by two-tailed unpaired t-test. ***$P$<=0.001.
949
950
951 **Figure 2 – WASp controls the deformation and integrity of the nucleus during migration in**
952 **microchannels**. (**A**) Analysis of nuclear parameters in macrophages migrating through 2-8 µm x 5
953 µm fibronectin coated micro-channels. Representative images of nuclei within channels after
954 overnight migration (applying a nuclear mask). (**B**) Entrance rate of the two genotypes inside
955 channels of different dimensions. Data are from *N*=3 and *N*=4 independent experiments for WT and
956 WKO, respectively. Data were analysed by two-way ANOVA test, *$P$<=0.05. (**C**) Representative
957 examples of WT and WKO macrophage nuclei inside 6 µm x 5 µm channels (left). Corresponding
958 quantification of the fraction of cells showing herniated nuclei (right). *n*=40 WT and 57 WKO cells in
959 *N*=3 independent experiment, two-tailed unpaired t-test. (**D**) Quantification of the position of the
960 herniation relative to the direction of migration, two-way ANOVA with Sidak's correction method.
961 ns, not significant. (**E**) WT and WKO BMDM were transduced with NLS-GFP to track nuclear rupture
962 during migration. (**F**) Representative time frames (top) and relative kymographs (bottom) showing a
963 nuclear rupture event in WKO migrating inside 6 µm x 5 µm channels, detected as cytosolic leakage
964 of NLS-GFP. Scale bar 10 µm. (**G**) Quantification of the fraction of cells undergoing nuclear rupture
965 during live imaging. *N*=3 independent experiments, with at least 20 individual cells analysed per
966 genotype for each experiment. Two-tails unpaired t-test. *$P$<=0.05. (**H**) Quantification of multiple
967 nuclear ruptures detected during live imaging experiments expressed as fraction of total ruptures
968 recorded.
969
970
971 **Supplementary Figure 2 – Constricted migration augments DNA damage in WKO cells**. (**A**)
972 Schematic overview of nuclear mask segmentation from raw channel images and quantification of
973 entrance rate as percent of cells inside channels and approaching cells. Approaching cells were
974 defined as those present within 50 µm from channel beginning (yellow dashed line). (**B**) Schematic

975 overview of transwell assay used for BMDCs migration (top) and relative quantification of
976 transmigrating cells (bottom), in transwell of indicated pore size. *N*=3 independent replicates are
977 plotted as normalized fold to respective WT (value=1). Statistics was calculated using a one-sample
978 t-test. (**C**) Representative pictures of γH2AX staining pre and post 3 µm transwell migration in BMDCs
979 and relative quantification of number of γH2AX foci per cell in WT and WKO. Data are from *N*=3
980 independent experiments with *n*=178; 202 (WT and WKO pre transwell) and *n*=13; 33 (WT and WKO
981 post transwell). **P*<=0.05 in a standard one-way ANOVA test. (**D**) Flow cytometry quantification of
982 CCR7 median expression in WT and WKO BMDCs before 3 µm transwell migration and following 200
983 ng/mL of LPS stimulation for 30' (*N*=3) or in unstimulated control (*N*=2). Statistics was performed
984 comparing WT and WKO after LPS stimulation by an unpaired t-test. ns, not significant.
985
986
987 **Figure 3 – Vertical confiners induce higher deformation and rupture in WASp-deficient**
988 **macrophages.**
989 (**A**). Examples of intact or damaged nuclei, as used for quantification. (**B**) Representative images of
990 WT and WKO macrophage's nuclei under 3 or 6 µm confinement height (right). Insets show nuclear
991 deformation. Scale bar 10 µm. Quantification of the fraction of cells carrying a damaged nucleus
992 after 1 h confinement at the indicated height (left). At least 200 cells per conditions were analysed
993 in *N*=3 independent experiments. Two-tailed unpaired t-test. ****P*<=0.001. (**C**) Assay on NLS-GFP
994 cytosolic release under confinement. Representative images of NLS-GFP$^+$ macrophages after 1h of
995 confinement at 3 µm. Scale bar 20 µm. (**D**) Corresponding quantification of nuclear ruptures upon
996 confinement based on NLS-GFP cytosolic leakage in C. Each dot is an independent experiment (*N*=3).
997 *n*=173 WT and *n*=102 WKO cells. Data are expressed as fold to WT mean. **P*<=0.05 in a two-tailed
998 unpaired t-test. (**E**) Individual frames from a live imaging experiment showing nuclear envelope
999 rupture during following bleb formation in WKO (yellow arrow). The timeframe is indicated by f. (**F**)
1000 Representative images of WASp-GFP$^+$ and WASp-GFP$^-$ macrophages after 1 h confinement at 3 µm.
1001 Dashed lines mark nuclear boundaries. Scale bar 20 µm; 5 µm for insets. (**G**) Corresponding
1002 quantification of nuclear blebbing in control or WASp-GFP reconstituted cells. Data are expressed as
1003 fold on WKO ctrl, *n*=83 WT and *n*=99 WKO cells from *N*=3 independent experiments, one sample t-
1004 test. ***P*<=0.01. (**H**). Representative images of confined (3µm) WASp-GFP$^+$ and WASp-GFP$^-$
1005 macrophages stained for Lamin A/C (yellow). Nuclear insets show Lamin A/C and Hoechst signal in
1006 WKO ctrl (1) and WKO WASp-GFP (2). Scale bar 20 µm. (**I**) Quantification of Lamin A/C rupture events

1007 in WKO ctrl and WKO WASp-GFP based on **H**. Data are from n=135 WKO ctrl and n=22 WKO WASp-
1008 GFP in *N*=2 experiments.
1009
1010
1011 **Supplementary Figure 3 – WASp limits nuclear rupture under confinement**. (**A**) Cells were
1012 subjected to vertical confinement, as schematically represented. (**B**) Nuclear height quantification in
1013 2D without confinement in BMDM. Data from *N*=1 experiment with a total of 10 z-stacks nuclei
1014 measured per genotype. (**C**) Representative images of BMDM nuclear height from live-imaging
1015 confocal acquisition of cell under confinement at 6 µm and 3 µm. Vertical scale bar 6 µm, with a tick
1016 every 1 µm. (**D**) WKO BMDM were transduced with lentiviral particles encoding WASp-GFP. (**E**) Flow
1017 cytometry shows the fraction of WKO cells expressing WASp-GFP to visualize WASp-GFP expression.
1018 (**F**) Representatives immunoblot of WASp expression in WT, WKO ctrl and WKO WASp-GFP
1019 macrophages after 7 days of differentiation.
1020
1021
1022 **Figure 4 – WASp triggers perinuclear actin polymerization under confinement**. (**A**) Representative
1023 images of actin distribution in WT and WKO BMDM confined at 3 µm height. Scale bars 20 µm. (**B**)
1024 Quantification of the fraction of cells with central actin accumulation. n=number of cells, as indicated
1025 in figure. *N*=2 experiments for unconfined controls and *N*=4 for confined samples. Two-tailed
1026 unpaired t-test. ***P*<=0.01. (**C**) Representative images to define patterns of actin distribution in
1027 macrophages confined at 3 µm. Scale bar 5 µm. (**D**) Corresponding quantification of the fraction of
1028 WT and WKO macrophages in each category. n=number of cells, as indicated in figure; from *N*=3
1029 individual experiments. (**E**) WKO cells transduced with WASp-GFP were confined at 3 µm and
1030 analysed to visualize the relative distribution of WASp and F-actin. Scale bar 5 µm. Line intensity
1031 profile of selected region showing the intensity distribution of WASp-GFP and phalloidin (bottom).
1032 (**F**) Quantification of WASp-GFP and F-actin Mander's coefficient of colocalization on perinuclear
1033 actin patches. Data are from **E**, with a total of *n*=20 cells analysed from *N*=2 independent
1034 experiments.
1035
1036
1037 **Supplementary Figure 4 – WASp perinuclear localization under confinement**.

1038 (**A**) WASp-GFP expressing cells were recorded during migration in 5 x 5 µm microchannels. (**B**) After
1039 fixation at the end of the recording period, WASp distribution was calculated by dividing the cell
1040 volume into three equal parts (top left). Average intensity map of WASp-GFP was obtained by
1041 normalizing and merging different cells from a fixed end time point analysis (bottom left). Data are
1042 from *n*=42 cells obtained in *N*=2 independent experiments. Representative line intensity profile of
1043 WASp-GFP signal (right).
1044
1045
1046 **Figure 5 – Mechanical confinement triggers innate activation in WASp KO macrophages**. (**A**) BMDM
1047 were subjected to 1 h confinement at 3 µm or kept in unconfined conditions and processed for RNA-
1048 seq and gene qPCR expression analysis. (**B**) Venn diagram of common and unique upregulated DEGs
1049 in WT and WKO BMDM confined at 3 µm as compared to their respective unconfined controls.
1050 Relevant processes and genes are highlighted. (**C**) Log2FC of commonly upregulated inflammatory
1051 genes by confinement in the two genotypes. (**D**) Z-score of branched actin signature across the two
1052 genotypes in unconfined and confined conditions (left). Normalized expression of relevant individual
1053 genes is showed as heatmap (right). (**E**) Z-score of nuclear mechanic signature across the two
1054 genotypes in unconfined and confined conditions (left). Normalized expression of relevant individual
1055 genes is showed as heatmap (right). (**F**) Z-score of NER induced inflammatory signature across the
1056 two genotypes in unconfined and confined conditions (left). Normalized expression of relevant
1057 individual genes is showed as heatmap (right). *P* in **D**, **E**, and **F** were calculated by one-way ANOVA
1058 test. **P*<=0.05, ***P*<=0.01, ***P*<=0.001. (**G**) Quantification of Il6 mRNA in confined WT and WKO
1059 BMDM after 1 h at indicated heights. *n*=6 for unconfined and 3 µm confined samples, *n*=4 for 6 µm
1060 confined samples. ***P*<=0.01 on a one-way ANOVA test. (**H**) Normalized expression of Il6 mRNA in
1061 WT ctrl and WT WASp KO BMDM. Data from 6 individual confinement replicates. (**I**) Normalized
1062 expression of Il6 mRNA in WKO ctrl and WKO STING KO BMDM from 4 individual confinement
1063 experiments. **P*<=0.05 on a one-sample t-test. (**J**) Model of WT and WKO macrophage response to
1064 confinement.
1065
1066
1067 **Supplementary Figure 5 – Mechanical confinement triggers innate activation in WASp KO**
1068 **macrophages**. (**A**) Venn diagram of differentially expressed genes between WT and WKO in
1069 unconfined resting condition. Relevant genes and processes are highlighted. (**B**) PCA analysis of

1070 BMDM unconfined controls and 3 µm confined samples from RNA-seq. (**C**) Venn diagram of DEGs
1071 downregulated by confinement in WT and WKO at 3 µm. Relevant genes are highlighted. (**D**) Z-score
1072 of Rac2 signature across the two genotypes in unconfined and confined conditions (left). Normalized
1073 expression of Sun2/RhoA/ROCK genes is showed as heatmap (right). (**E**) Representative western blot
1074 of KO efficiency control in WT macrophages after 72 h from sgCtrl or sgWASp CRISPR-Cas9
1075 electroporation. (**F**) Representative western blot for KO efficiency in WKO macrophages after sgCtrl
1076 or sgSTING CRISPR-Cas9. (**G**) Il6 quantification in WKO and WKO STING KO at steady state and upon
1077 direct STING stimulation by 3 µg/mL of DMXAA.
1078
1079
1080 **Figure 6 – WASp deficiency correlates to enhanced expression of inflammatory genes in**
1081 **macrophages**. (**A**) Alveolar macrophages (AMO) from 10 weeks old mice were harvested and
1082 processed for flow cytometry. Data show mean fluorescent intensity (MFI) of CD86 from one
1083 representative of two experiments (*n*=3 mice per genotype). Two-tailed unpaired t-test; ***P*<=0.01.
1084 (**B**) Quantification of AMO total numbers in 10- and 25-weeks-old adult mice (*n*=3 mice, data are
1085 from one representative of two experiments). One-way ANOVA test with multiple comparisons,
1086 **P*<=0.05. (**C**) Il6 expression in AMO. mRNA expression (RT-qPCR, plotted as fold to WT) of the
1087 indicated genes in sorted AMO from 10-and 25-weeks-old WKO mice. *n*=3 mice for each condition,
1088 one sample t-test, **P*<=0.05. (**D**) Expression of inflammatory signature in WASp proficient (WASp +)
1089 or WASp null (WASp -) human iPSCs-derived macrophages from GSE107963 dataset. (**E**) Heatmap
1090 of NER inflammatory genes expression (Log2+1 TPM normalized expression, z-score gene-wise
1091 scaled) of WT and WASp null iPSCs-derived macrophages from GSE107963. (**F**) Heatmap of genes
1092 related to nuclear mechanics (Log2+1 TPM normalized expression, z-score gene-wise scaled) of WT
1093 and WASp null iPSCs-derived macrophages from GSE107963. (**G**) Inflammatory score in PBMCs of a
1094 cohort of 6 WAS patients before (WASp -) and after restoration of WASp by gene therapy (WASp +,
1095 post-GT). (**H**) Heatmap of NER inflammatory genes expression (Log2+1 normalized reads, z-score
1096 gene-wise scaled) in human PBMCs from WAS patients pre- and post- gene therapy. Normalized Δ
1097 NER score is represented by bar graph (bottom).
1098
1099
1100 **Supplementary Figure 6 - WASp reduces steady state inflammatory activation of macrophages in-**
1101 **vivo and in-vitro**. (**A**) Flow cytometry gating strategy to identify AMO in mouse lung tissues. (**B**) GSEA

1102 analysis of relevant modulated pathways in WAS PBMCs before and after gene therapy correction.
1103 Values are expressed as normalized enrichment score. (**C**) Expression of the indicated genes in
1104 individual PBMC samples pre- and post-gene therapy. Data are plotted as Log2 FC post vs pre gene
1105 therapy, each dot is a patient. One sample t-test; *$P$<=0.05 and **$P$<=0.01. (**D**) RT-qPCR validation
1106 of selected inflammatory genes in 6 WAS patients pre- and post-gene therapy. The dotted line
1107 represents the mean gene expression of 3 healthy donor controls (HC). One sample t-test: *$P$<=0.05.
1108 (**E**) Correlation between inflammatory score (IS) before WASp restoration (y-axis) and IS reduction
1109 (Δ IS) upon WASp re-expression (x-axis). Data combines 3 human iPSCs-derived macrophages and 6
1110 human PBMCs. Data were analysed by linear regression; $P$=0.0095.
1111
1112
1113

# Figure 1

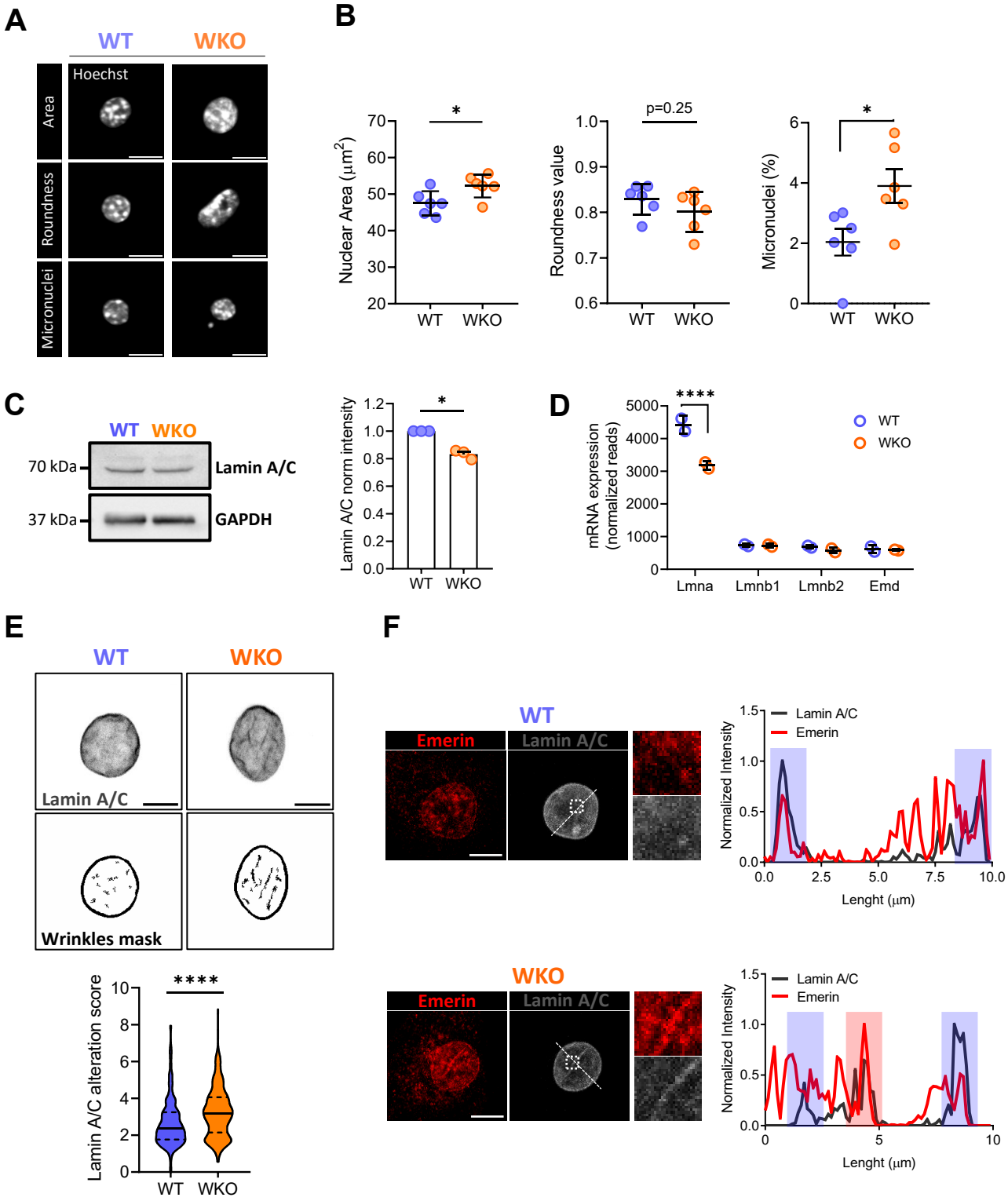
A
WT
WKO
Hoechst
Area
Roundness
Micronuclei
B
Nuclear Area (μm²)
Roundness value
Micronuclei (%)
p=0.25
WT
WKO
C
WT
WKO
70 kDa
Lamin A/C
37 kDa
GAPDH
Lamin A/C norm intensity
D
mRNA expression (normalized reads)
WT
WKO
Lmna
Lmnb1
Lmnb2
Emd
E
WT
WKO
Lamin A/C
Wrinkles mask
Lamin A/C alteration score
F
WT
Emerin
Lamin A/C
Normalized Intensity
Lenght (μm)
WKO

# Supplementary Figure 1

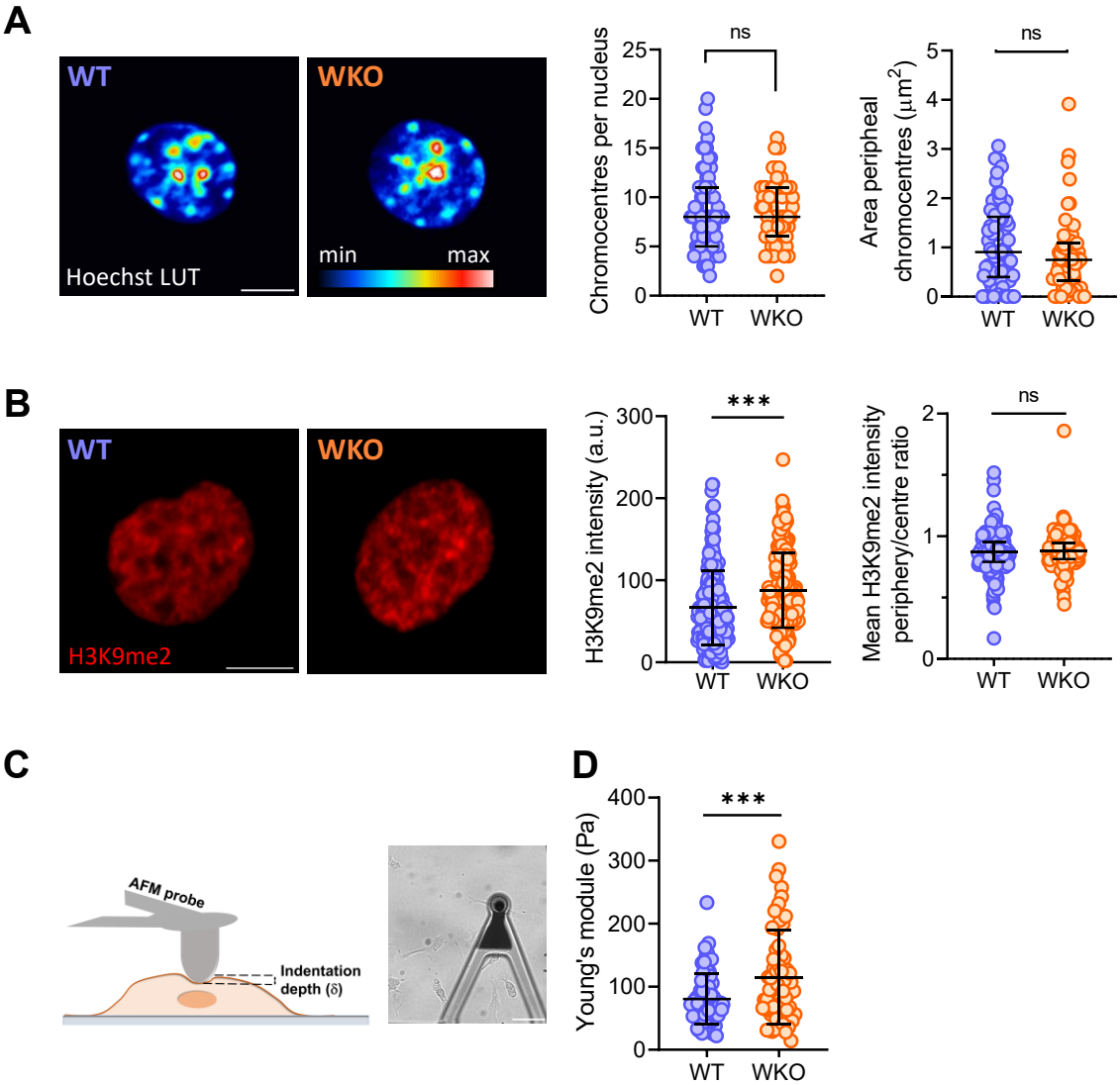

# Figure 2

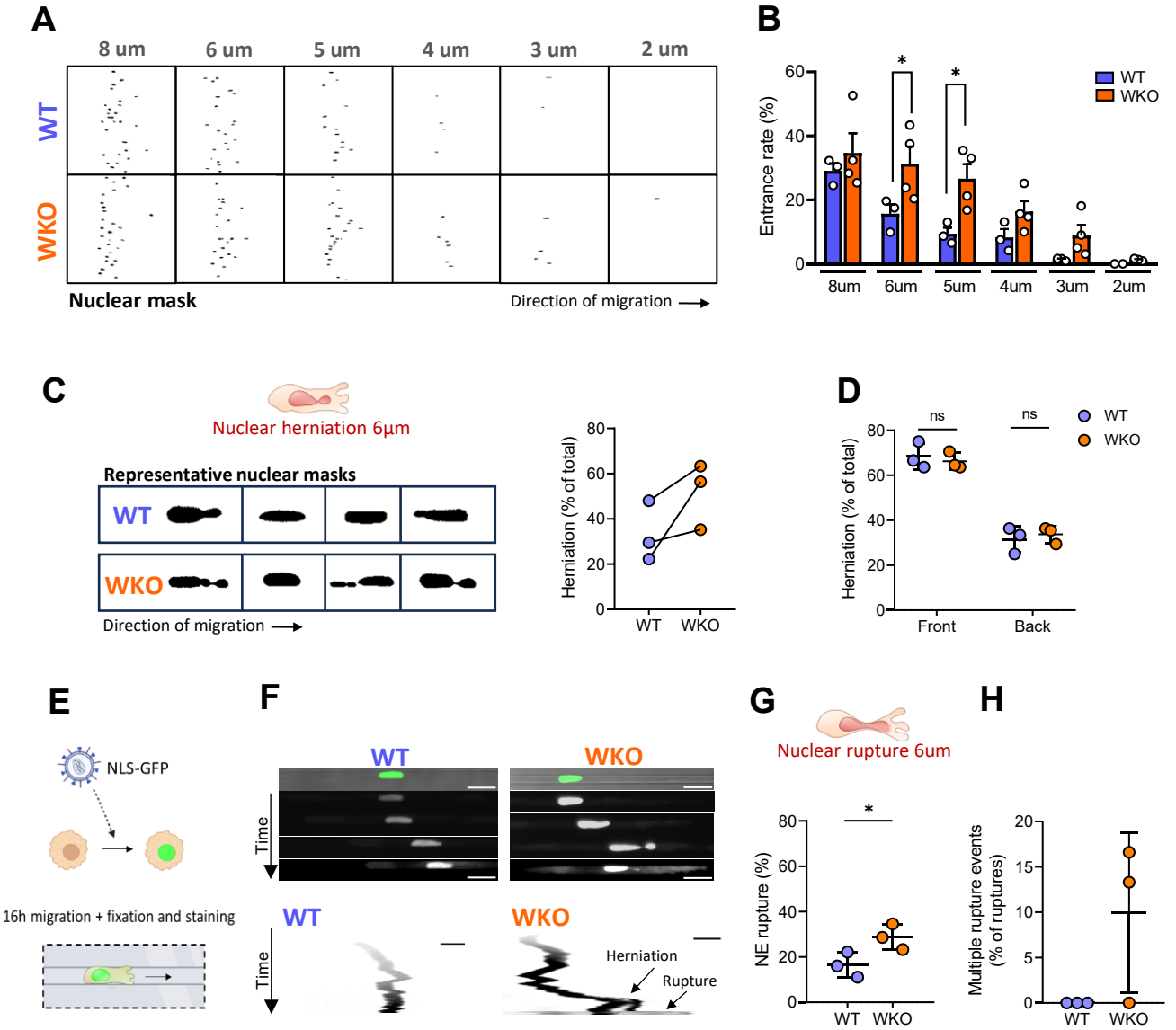
A
8 um
6 um
5 um
4 um
3 um
2 um
WT
WKO
Nuclear mask
Direction of migration
B
Entrance rate (%)
WT
WKO
8um
6um
5um
4um
3um
2um
C
Nuclear herniation 6µm
Representative nuclear masks
WT
WKO
Direction of migration
Herniation (% of total)
WT
WKO
D
ns
ns
Herniation (% of total)
WT
WKO
Front
Back
E
NLS-GFP
16h migration + fixation and staining
F
WT
WKO
Time
Herniation
Rupture
G
Nuclear rupture 6um
NE rupture (%)
WT
WKO
H
Multiple rupture events (% of ruptures)
WT
WKO

# Supplementary Figure 2

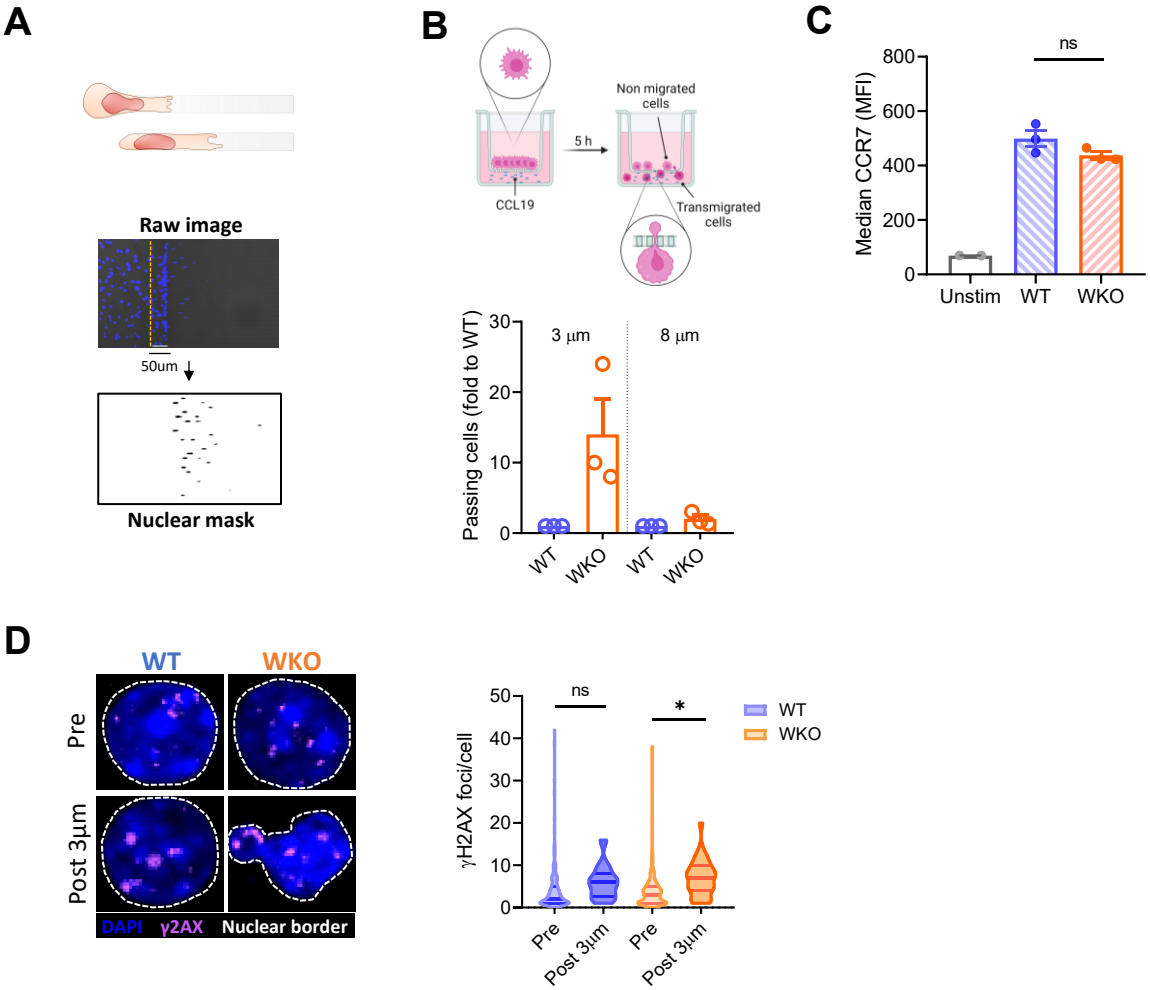

# Figure 3

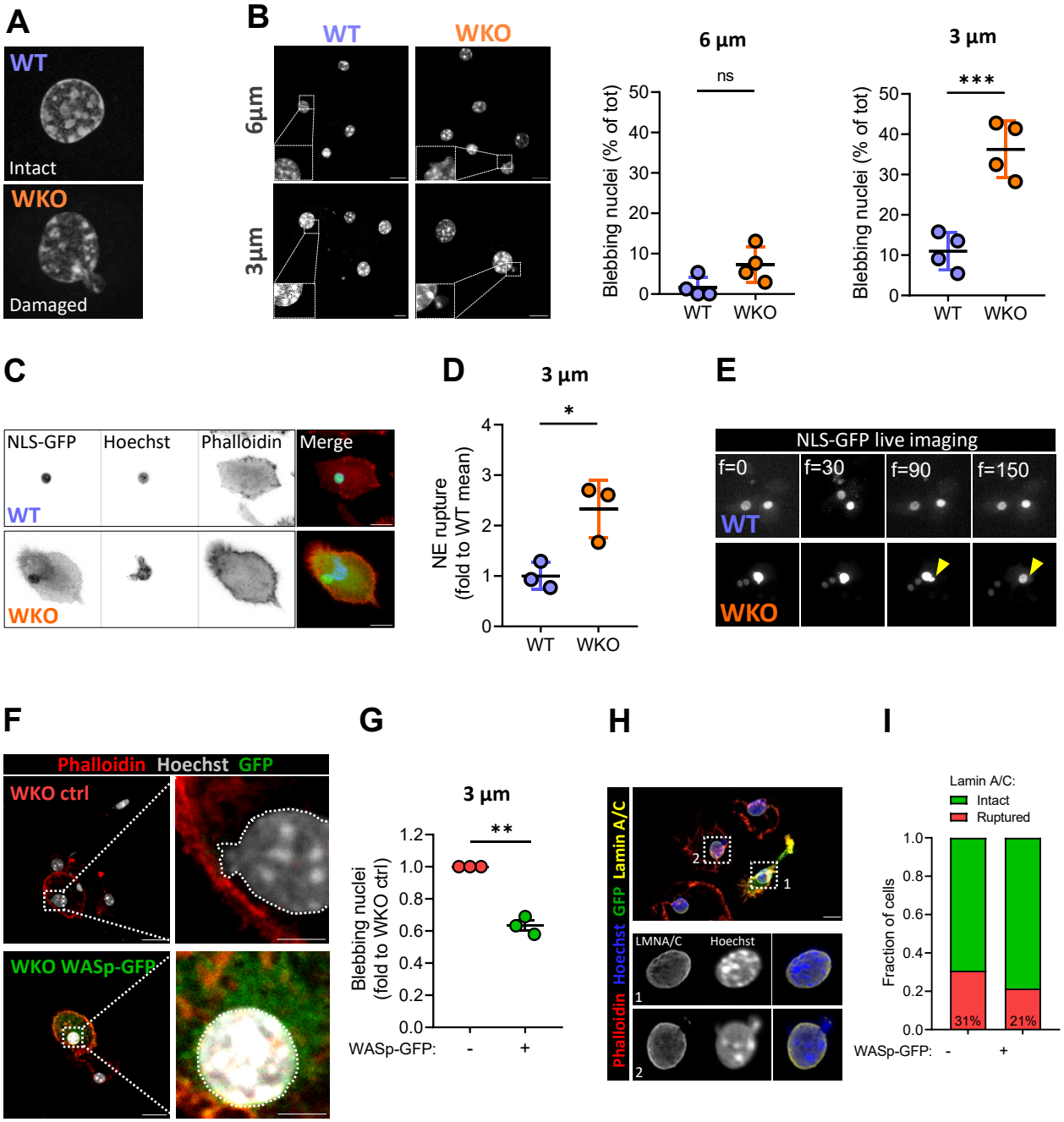
A
WT
Intact
WKO
Damaged
B
WT
WKO
6µm
3µm
6 µm
ns
Blebbing nuclei (% of tot)
50
40
30
20
10
0
WT
WKO
3 µm
***
Blebbing nuclei (% of tot)
50
40
30
20
10
0
WT
WKO
C
NLS-GFP
Hoechst
Phalloidin
Merge
WT
WKO
D
3 µm
*
NE rupture
(fold to WT mean)
4
3
2
1
0
WT
WKO
E
NLS-GFP live imaging
f=0
f=30
f=90
f=150
WT
WKO
F
Phalloidin Hoechst GFP
WKO ctrl
WKO WASp-GFP
G
3 µm
**
Blebbing nuclei
(fold to WKO ctrl)
1.2
1.0
0.8
0.6
0.4
0.2
0.0
WASp-GFP:
-
+
H
Phalloidin Hoechst GFP Lamin A/C
2
1
LMNA/C
Hoechst
1
2
I
Lamin A/C:
Intact
Ruptured
Fraction of cells
1.0
0.8
0.6
0.4
0.2
0.0
31%
21%
WASp-GFP:
-
+

# Supplementary Figure 3

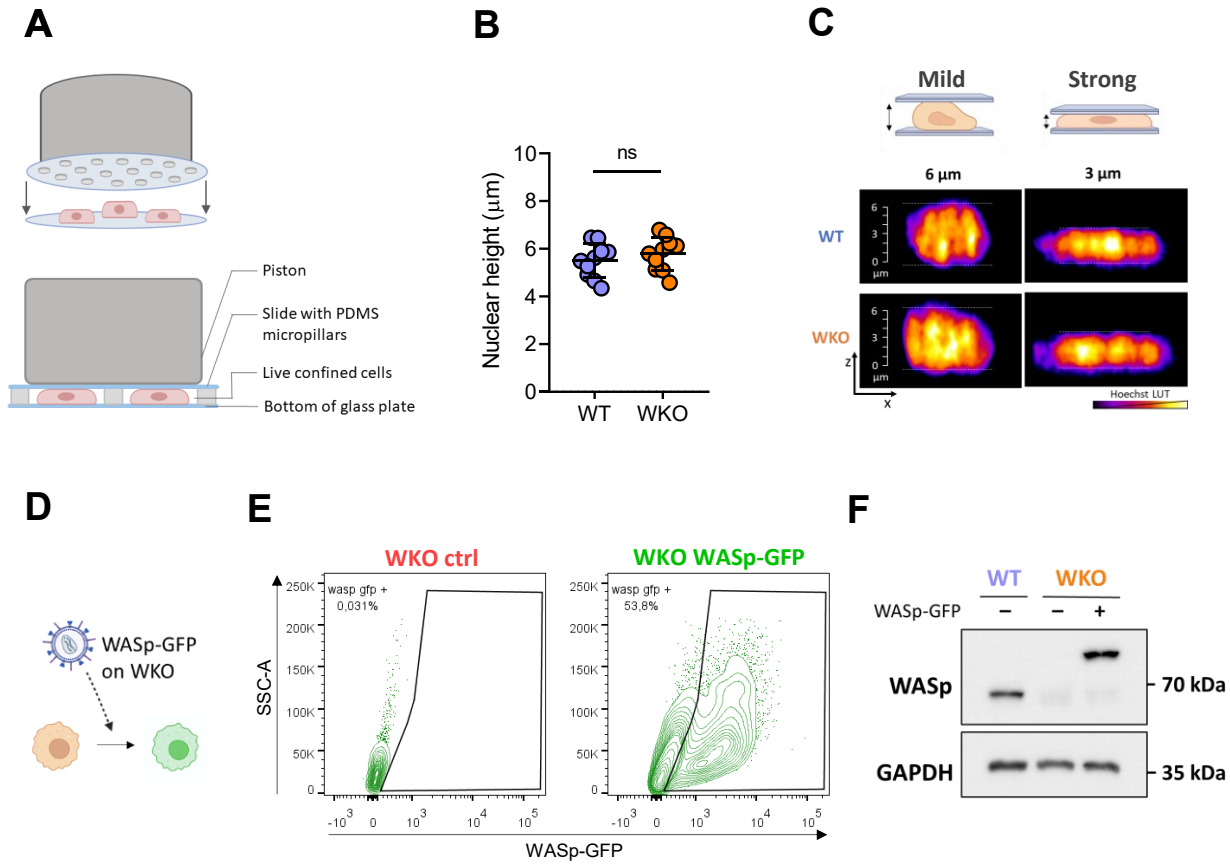

# Figure 4

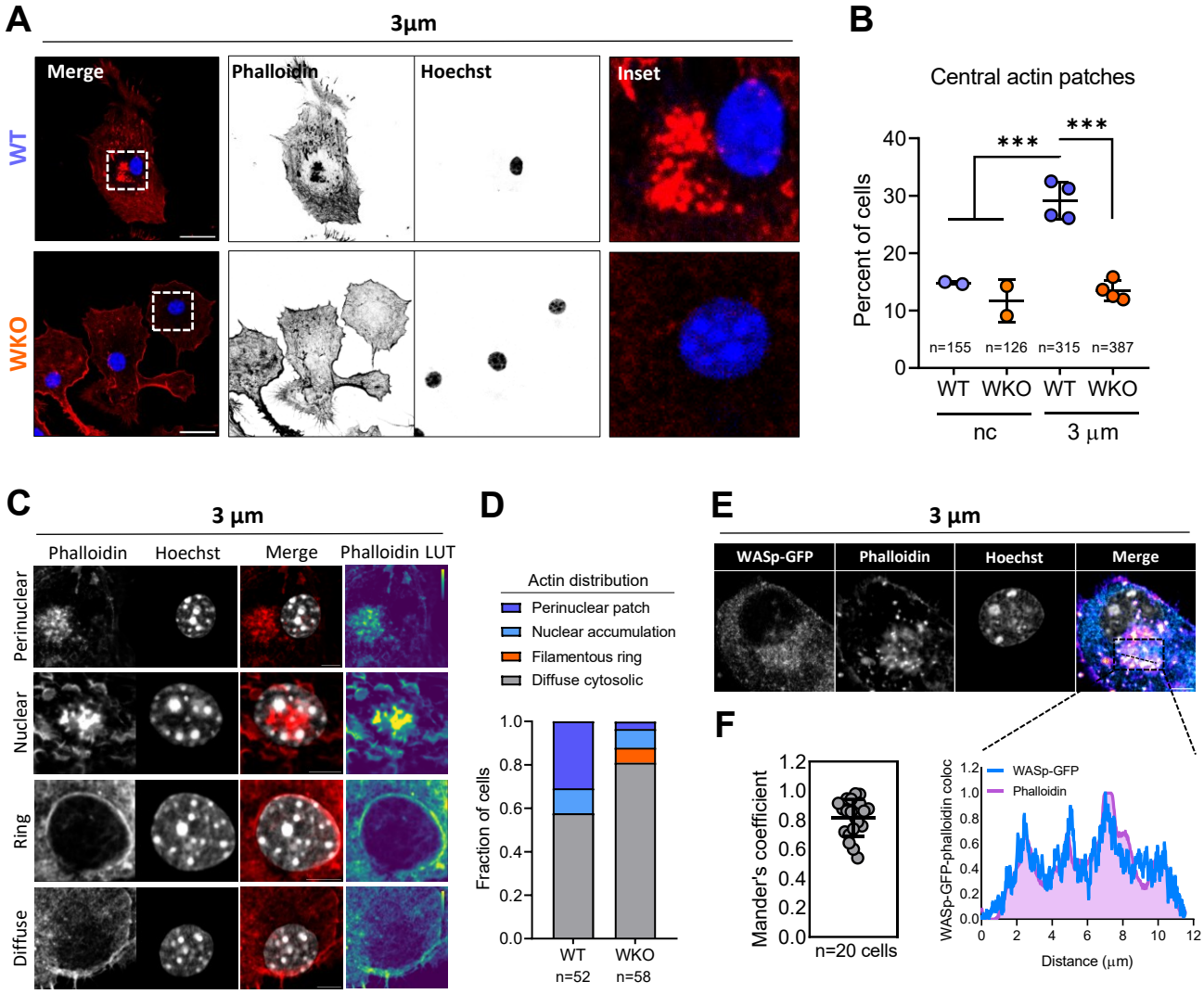
A
3µm
Merge
Phalloidin
Hoechst
Inset
WT
WKO
B
Central actin patches
Percent of cells
***
***
n=155
n=126
n=315
n=387
WT
WKO
WT
WKO
nc
3 µm
C
3 µm
Phalloidin
Hoechst
Merge
Phalloidin LUT
Perinuclear
Nuclear
Ring
Diffuse
D
Actin distribution
Perinuclear patch
Nuclear accumulation
Filamentous ring
Diffuse cytosolic
Fraction of cells
WT
n=52
WKO
n=58
E
3 µm
WASp-GFP
Phalloidin
Hoechst
Merge
F
Mander's coefficient
n=20 cells
WASp-GFP-phalloidin coloc
WASp-GFP
Phalloidin
Distance (µm)

# Supplementary Figure 4

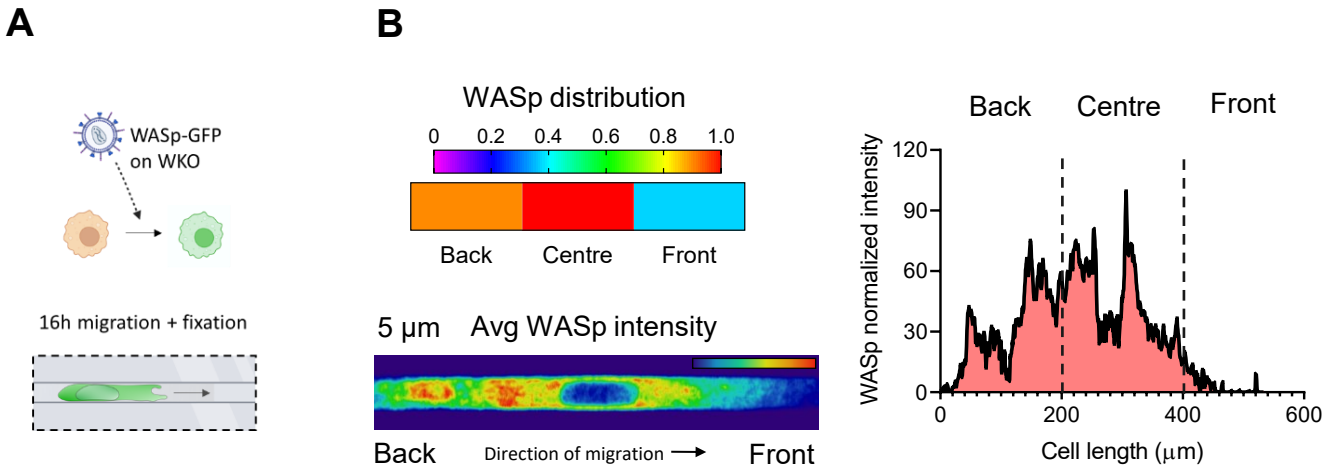

# Figure 5

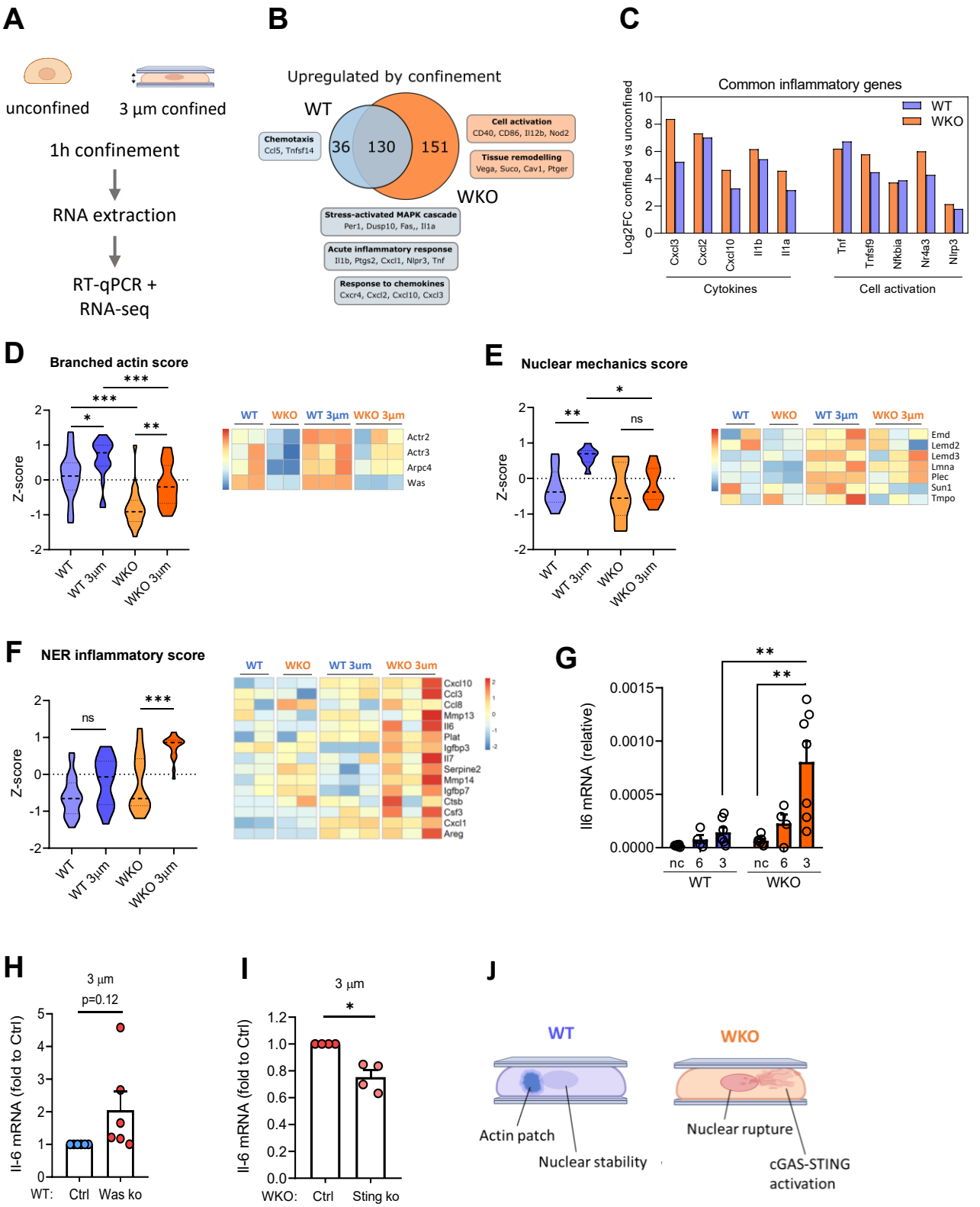
A
unconfined
3 µm confined
1h confinement
RNA extraction
RT-qPCR +
RNA-seq
B
Upregulated by confinement
WT
WKO
36
130
151
Chemotaxis
Ccl5, Tnfsf14
Cell activation
CD40, CD86, Il12b, Nod2
Tissue remodelling
Vega, Suco, Cav1, Ptger
Stress-activated MAPK cascade
Per1, Dusp10, Fas,, Il1a
Acute inflammatory response
Il1b, Ptgs2, Cxcl1, Nlpr3, Tnf
Response to chemokines
Cxcr4, Cxcl2, Cxcl10, Cxcl3
C
Common inflammatory genes
Log2FC confined vs unconfined
WT
WKO
Cxcl3
Cxcl2
Cxcl10
Il1b
Il1a
Tnf
Tnfsf9
Nfkbia
Nr4a3
Nlrp3
Cytokines
Cell activation
D
Branched actin score
Z-score
WT
WT 3µm
WKO
WKO 3µm
Actr2
Actr3
Arpc4
Was
E
Nuclear mechanics score
Z-score
ns
Emd
Lemd2
Lemd3
Lmna
Plec
Sun1
Tmpo
F
NER inflammatory score
Z-score
ns
WT 3um
WKO 3um
Cxcl10
Ccl3
Ccl8
Mmp13
Il6
Plat
Igfbp3
Il7
Serpine2
Mmp14
Igfbp7
Ctsb
Csf3
Cxcl1
Areg
G
Il6 mRNA (relative)
nc
6
3
WT
WKO
H
3 µm
p=0.12
Il-6 mRNA (fold to Ctrl)
WT:
Ctrl
Was ko
I
3 µm
Il-6 mRNA (fold to Ctrl)
WKO:
Ctrl
Sting ko
J
WT
WKO
Actin patch
Nuclear stability
Nuclear rupture
cGAS-STING
activation

# Supplementary Figure 5

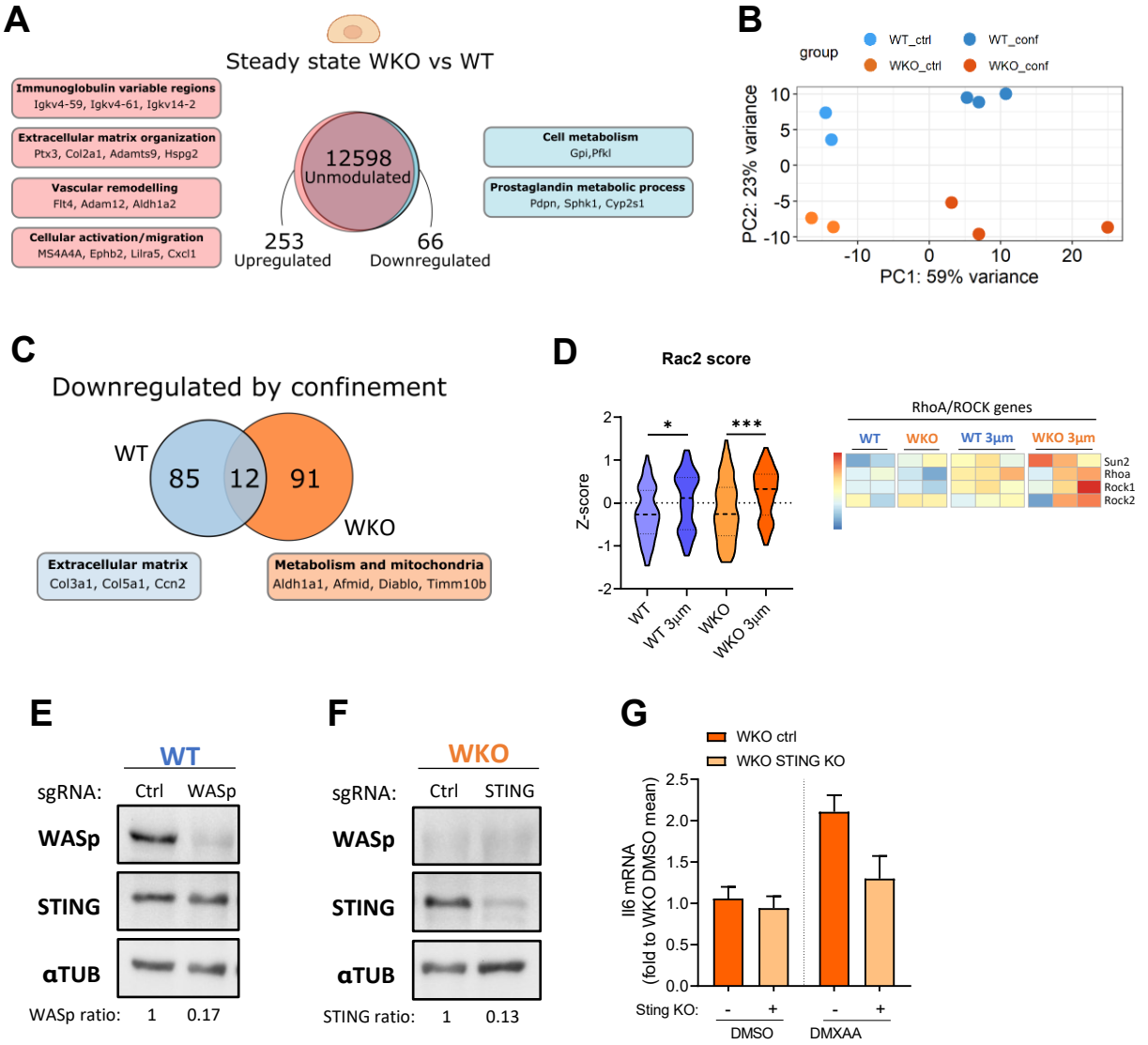

# Figure 6

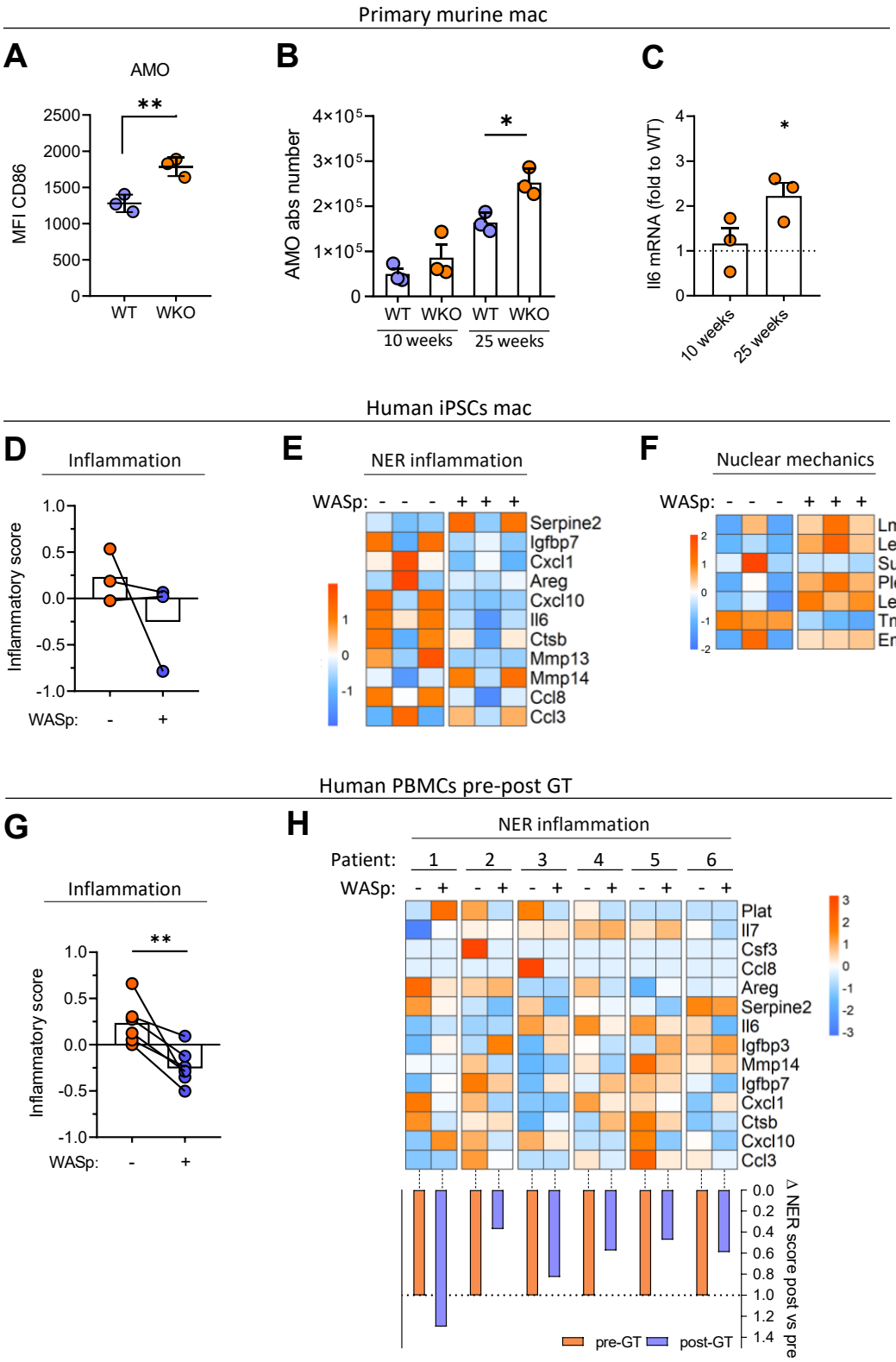
Primary murine mac
A
AMO
MFI CD86
2500
2000
1500
1000
500
0
**
WT
WKO
B
AMO abs number
4×10⁵
3×10⁵
2×10⁵
1×10⁵
0
*
WT
WKO
WT
WKO
10 weeks
25 weeks
C
Il6 mRNA (fold to WT)
4
3
2
1
0
*
10 weeks
25 weeks
Human iPSCs mac
D
Inflammation
Inflammatory score
1.0
0.5
0.0
-0.5
-1.0
WASp:
-
+
E
NER inflammation
WASp:
- - - + + +
Serpine2
Igfbp7
Cxcl1
Areg
Cxcl10
Il6
Ctsb
Mmp13
Mmp14
Ccl8
Ccl3
1
0
-1
F
Nuclear mechanics
WASp:
- - - + + +
Lmna
Lemd2
Sun1
Plec
Lemd3
Tmpo
Emd
2
1
0
-1
-2
Human PBMCs pre-post GT
G
Inflammation
Inflammatory score
1.0
0.5
0.0
-0.5
-1.0
**
WASp:
-
+
H
NER inflammation
Patient:
1
2
3
4
5
6
WASp:
- + - + - + - + - + - +
Plat
Il7
Csf3
Ccl8
Areg
Serpine2
Il6
Igfbp3
Mmp14
Igfbp7
Cxcl1
Ctsb
Cxcl10
Ccl3
3
2
1
0
-1
-2
-3
Δ NER score post vs pre
0.0
0.2
0.4
0.6
0.8
1.0
1.2
1.4
pre-GT
post-GT
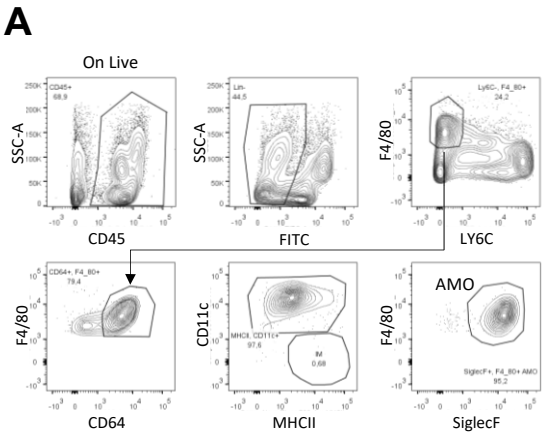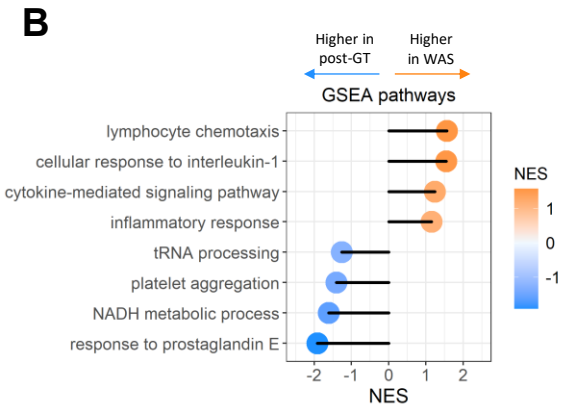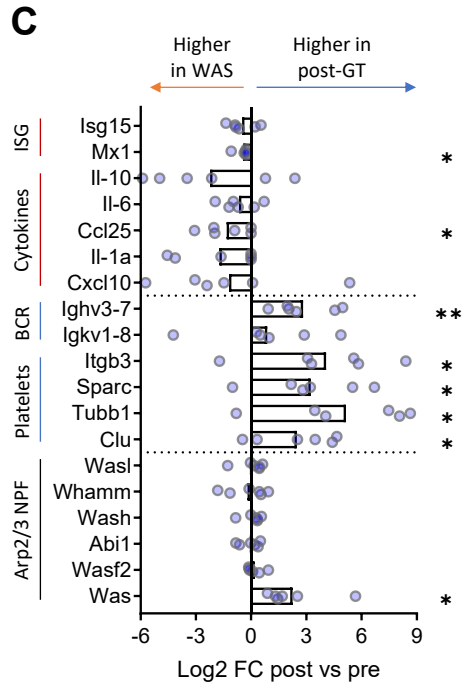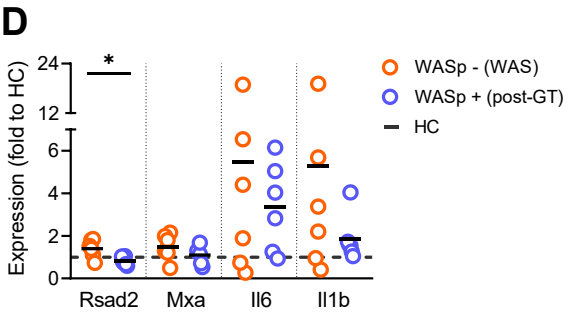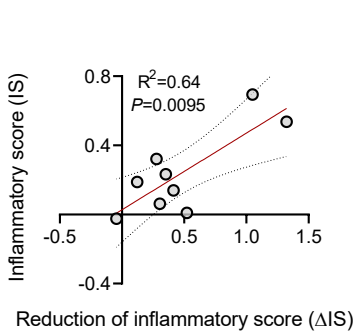
# Supplementary Figure 6